Aalto University
School of Chemical
Engineering

Master's Programme in Chemical, Biochemical and Materials Engineering

Nicholas Ewiene Addy-Tayie

FABRICATION OF SUPERHYDROPHOBIC GLASS CAPILLARIES

Thesis Supervisor: Professor Sami Franssila

Thesis Advisors: Dr Ville Jokinen

MSc Seyed Mehran Mirmohammadi

Master's Thesis
2023

Author Nicholas Ewiene Addy-Tayie

Title of thesis Fabrication of Superhydrophobic Glass Capillary

Programme Chemistry and Materials Science

Major Functional Materials (CHEM3025)

Thesis supervisor Professor Sami Franssila

Thesis advisor(s) Dr Ville Jokinen and Seyed Mehran Mirmohammadi

Date 02.02.2023 **Number of pages** 61 **Language** English

Abstract

This thesis presents the fabrication of superhydrophobic glass capillaries with water contact angles >168˚, contact angle hysteresis <1˚ and water droplet sliding angle <10˚ through a three-step fabrication approach: ALD deposition of Al_2O_3 film, hydrothermal treatment to produce Al_2O_3 nanograss and silane coating of the nanograss.

The fabricated superhydrophobic glass capillaries retained their transparency and provided drag reduction when compared to the as received capillaries which served as controls. They provided reduced droplet sliding angles and improved water flow rates in hydraulic drag resistance testing. It was demonstrated through hydraulic testing that, the lowered drag resistance was higher at low Reynolds numbers, where reductions of over 40% were achieved.

The superhydrophobic capillaries also exhibited bio-repellency, as they provided lower droplet sliding angles of protein solution bovine serum albumin (BSA).

The characterization of the fabricated glass capillaries indicated that the adopted fabrication method was successful in creating superhydrophobic surface on the inner walls of glass capillaries with aspect ratio (length to inner diameter) of up to 25.

Keywords Atomic layer deposition, hydrothermal treatment, Al_2O_3 nanograss, SAM treatment, aspect ratio, droplet sliding angle, Reynolds number.

Acknowledgements

I would like to express my great appreciation to Professor Sami Franssila, my thesis supervisor, for accepting me into his research group, and giving me the opportunity to learn under him. He always created a conducive learning environment and provided me with professional guidance throughout my work.

I want to give thanks to my thesis advisors Dr Ville Jokinen and Seyed Mehran Mirmohammadi. They devoted their knowledge and time to proffer constructive suggestions and insightful comments to help make this thesis a possibility.

Special thanks to Dr Christoffer Kauppinen for his expertise and the time devoted to the ALD fabrication. His informed suggestions and guidance are much appreciated.

I would also like to acknowledge Micronova for providing the laboratory facilities such as the Cleanroom and Thin film lab that were used in the fabrications and characterizations for this Thesis.

Finally, I want to thank my family and my partner Pamela Blay for the love and care that kept me sane and capable.

Table of Contents

List of Symbols

γ Surface tension

θ_Y Contact angle

θ_{adv} Advancing contact angle

θ_{rec} Receding contact angle

r_w Roughness factor

θ_w Actual rough surface

° Degree

°C Degree Celsius

K_c Capillary length

f_s Area fraction of solid

f_V Area fraction of gas

Re Reynolds number

μ Fluid viscosity

H_f Hydrostatic force

H_p Hydrostatic pressure

A_c Cross-sectional area of capillary

E_a Activation barrier

F_{dr} Driving force

List of Abreviations

ALD	Atomic layer desposition
AZO	Aluminium doped zinc oxide
BSA	Bovine serum albumin
CA	Contact angle
CVD	Chemical vapor deposition
DIW	Deionized water
GPC	Growth per cycle
LPEI	Linear polyethyleneimine
LV	Liquid-gas interface
OTS	Octadecyltrichlorosilane
PBS	Phosphate-buffered saline
PDMS	Polydimethylsiloxane
PFOTS	Perfluorooctyl triethoxysilane
SAM	Self-assembly monolayers
SEM	Scanning electron Microscopy
SHB	Superhydrophobic
SL	Solid-liquid interface
SV	Solid-gas interface
TMA	Trimethylaluminum

1 Introduction

Micro-nano structures on surfaces of naturally existing objects such as the surfaces of the lotus-leaf and water strider legs have provided conceptual phenomenon for the fabrication of artificial superhydrophobic (SHB) surfaces [1, 2]. These surfaces exhibit desirable properties such as their ability to stay dry, self-clean and avoid biofouling [2, 3]. Such properties make them effective in applications involving lossless liquid transfer in several industrial operations as well as medicine and biotechnology. The self-cleaning property makes them desirable for outdoor optical devices like satellite dishes, display panels, vehicle wind shields and solar panels [4]. They are also effective in fog harvesting and surfaces for anti-icing [3, 5-7].

Thomas Young formulated a relation between the surface tensions of the droplet, solid surface, and surrounding air as determinant factors for the contact angle of the droplet on the surface or wettability [2, 4]. However, his study was based on ideal smooth surface, which is rarely the case. Consequently, Cassie and Baxter modified the Young's relation or equation to factor in the chemical and physical conditions of an actual material surface – which is mostly rough. Hence, superhydrophobicity is also termed Cassie-Baxter wetting state. [2, 4].

A superhydrophobic surface shows high mobility of liquid droplet because the droplet cannot wet the surface [2]. Figure 1 shows different forms of surface wetness depending on the physical and chemical composition of the surface: flat surface, nanostructure asperities,Figure 1 microstructure bumps and hierarchical structures. Total surface wetness can be achieved with flat surfaces, while surface repellence or non-wetness can be achieved with high level of roughness which is provided by the hierarchical structures. The hierarchical structures have double-scale roughness, i.e., the combination of the micro-sized bumps with nano-sized asperities, for the most effective air entrapment leading to the most reduction in contact area of the applied liquid droplet [1].

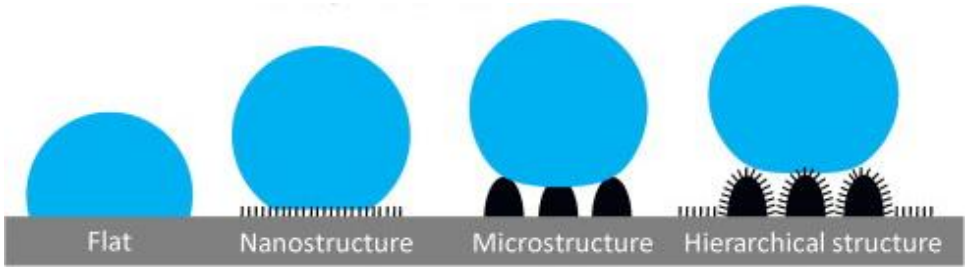

Figure 1: Schematic of wetting behavior on four different surface structures. Total surface wetness is achieved with flat surfaces while surface repellence can be achieved with higher level of surface roughness like the hierarchical structure. Hierarchical structure is a combination of both microstructure bumps with nanostructure asperities to provide the best conditions for superhydrophobicity [1].

Chemical modification to lower the surface energy of such hierarchical structures leads to the establishment of superhydrophobic conditions by producing larger static contact angle, smaller contact angle hysteresis and a reduction in adhesive force between liquid droplet and the solid surface [1, 3, 4, 8].

The absolute majority of superhydrophobic surface fabrication is based on planar surfaces, because fabrication on curved and closed surfaces are more difficult [9]. Fabrication on curved and closed surfaces is achieved by highly conformal method of fabrication. This method must adequately distribute the surface modification agent across the desired curved area, without compromising the overall shape of the substrate material. In this regard, fabrication of SHB surface on curved surfaces have not received much attention as compared to planar surfaces [9]. However, SHB surfaces on curved surfaces such as the inner wall of glass capillaries can improve efficiency in fluidics and heat transfers [9, 10]. Also, achieving surface superhydrophobicity with some level of glass transparency can be useful in fluidic transfer in medicine where transfer progress observation can be necessary [9].

Chapter 2 of this Thesis focuses on the concept of superhydrophobicity. Chapter 3 discusses the steps involved in fabricating superhydrophobic layers on arbitrary surfaces. Chapter 4 focuses on superhydrophobic

capillaries or tubes, some fabrication methods and fluidic performance in capillaries. Chapter 5 presents the experimental processes of this Thesis work, which includes the materials and methods, the fabrication processes, surface characterization techniques and fluidic performance evaluation. Chapter 6 presents the results and discussions of the experimental processes. Finally, Chapter 7 focuses on future outlooks as a result of observations made during this work and concluding remarks.

At the end of this work, SHB coating is introduced on to the inner walls of 6 mm, 4 mm and 0.6 mm inner diameter glass capillaries at 100 mm long. The SHB capillaries show improved fluidic performances. For instance, the water sliding angles (SA) with 500 μL droplet, of the largest SHB capillaries with 6 mm inner diameter was 2.5°, whereas 18° was recorded from the corresponding control capillaries. Also, these SHB capillaries exhibited 4% higher flow rate, and hence, higher Reynolds number relative to the control capillaries. Dynamic contact angle of the SHB coating produces advancing contact angle >169° and a receding contact angle >168° with a contact angle hysteresis <1°.

2 Superhydrophobicity

Superhydrophobic (SHB) surfaces are defined as exhibiting static water contact angle (CA) of over 150° with contact angle hysteresis less than 5° and rolling angle less than 10° [1-3, 5].

During surface wettability measurement, a solid-liquid-vapor interface becomes predominant on the droplet after contact with a solid surface. The shape of a liquid droplet is determined by the surface tension (γ) at the liquid-gas or vapor interface (γ_{LV}) and gravity [4]. The surface tension force acting on the droplet imposes minimal surface area causing a spherical droplet to be formed. On the other hand, the gravitation force which is dependent on the density of the liquid (ρ) and gravitation constant (g) tends to flatten the liquid droplet [4].

However, this gravitational force can be regarded as negligible and ignored if the droplet size is smaller than the capillary length [4]. Capillary length K_c is given as:

$$K_c = \sqrt{\frac{\gamma_{LV}}{\rho g}} \qquad 1$$

Where K_c is the capillary length, γ_{LV} is the surface tension of the liquid-gas interface, ρ is density of the liquid and g is acceleration due to gravity. The capillary length K_c of clean water is about 2.7 mm [4].

Figure 2 shows the various surface tension forces (solid-liquid (γ_{SL}) phase, liquid-gas (γ_{LV}) phase and solid-gas (γ_{SV}) phase) that act on the triple phase contact line [2, 4].

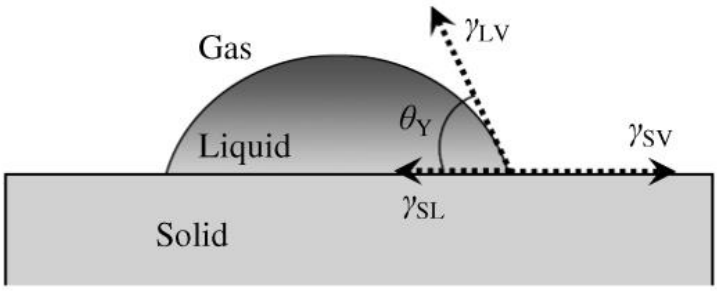

Figure 2: The three interfaces present around liquid droplet on an ideal smooth solid substrate. An equilibrium relation or Young's equation is derived by balancing the interfacial tensions on the tangential direction [4].

Each of these interfaces draws contact lines to minimize the total surface free energy [4]. The balancing of the surface tensions among these interfaces yields an equilibrium relation as established in 1805 by Thomas Young as the Young's equation, is shown in equation 2 below :

$$cos\theta_Y = \frac{\gamma_{SV} - \gamma_{SL}}{\gamma_{LV}} \qquad 2$$

In the equation 2, θ_Y represents the static contact angle of ideal smooth surface or Young's contact angle; γ is the surface tension, *SV* represents solid-gas interface, *SL* is solid-liquid interface and *LV* is liquid-gas interface. Hence, the smaller the surface tension of the solid component γ_{SV}, the bigger the Young's contact angle [2].

Young's equation as discussed above only applies to ideal smooth surfaces, but actual surfaces of most materials have some level of roughness. Therefore, in 1936 Wenzel studied the influence of the presence of surface roughness or textures on the wettability of droplets. He discovered that there is increase in the effective surface area because of the surface roughness. He therefore introduced a dimensionless roughness factor (r_w). This factor is the ratio of the actual surface area to the nominal or apparent surface area [4]. The roughness factor was introduced in Young's equation to form Wenzel's equation in equation 3 below in estimating the static contact angle of actual rough surface (θ_w) [2, 4]:

$$cos\theta_{\mathrm{W}} = r_w\left(\frac{\gamma_{\mathrm{SV}} - \gamma_{\mathrm{SL}}}{\gamma_{\mathrm{LV}}}\right) = \quad r_w \cos\theta_{\mathrm{Y}} \qquad 3$$

Wenzel's equation in equation 3 is the product of Young's equation (equation 2) and the surface roughness factor (r_w). It can be deduced from equation 3 that the surface roughness makes inherently hydrophobic surfaces more hydrophobic and inherently hydrophilic surfaces more hydrophilic. The relation was established on the assumption that the water droplet on a surface conformally fills the surface texture as seen in the Wenzel's model in Figure 3A. Therefore, a clear pathway for achieving superhydrophobicity is proposed: fabricate as much surface roughness as possible on a hydrophobic surface until the desired contact angle is recorded [2].

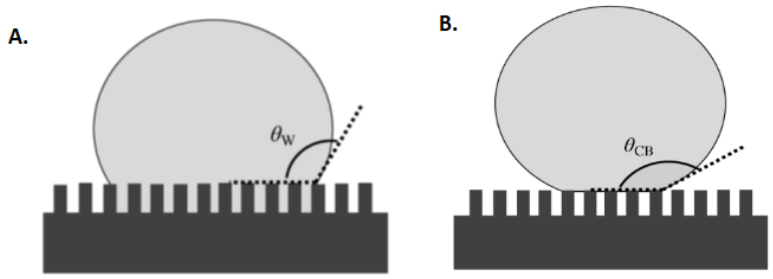

Figure 3: Surface wetting mechanism demonstrated by (a) Wenzel model and (b) Cassie-Baxter model. The Wenzel model produces relatively smaller static contact angle θ_W because it permits the liquid droplet to conformally follow the surface topography to cause wetting. Meanwhile, the Cassie-Baxter model produces relative larger contact angle θ_{CB} because it prevents wetting within the nanostructures by entrapping enough air to form surface shield against the droplet. [4].

In a dynamic contact angle (CA) measurement, the difference between advancing CA and the receding CA is termed as CA hysteresis [11]. Determining the CA hysteresis of a superhydrophobic surface with Wenzel's equation is not reliable [2]. This is because according to Wenzel's model as seen in Figure 3A, the droplet tends to completely wet the rough structures,

indicating a stronger adhesion between the droplet and the surface [2]. Therefore, the original Young's equation was modified again by Cassie and Baxter in 1944 [2, 4, 12]. This time, the diverse chemical composition present on the surface were considered in deriving a Cassie-Baxter equation in equation 4 [12]:

$$cos\theta_{CB} = f_s cos\theta_Y + f_V cos\theta_{LV} = f_s cos\theta_Y + f_s - 1 \qquad 4$$

In equation 4, θ_{CB} represents the static contact angle of the solid surface, the area fractions are represented by f_s for the solid and f_V for the gas or air which contains the liquid, θ_Y is the intrinsic contact angle of the solid and θ_{LV} is the intrinsic contact angle of the surrounding air. Considering that the spaces between the rough surface of a solid is filled with air, and since the intrinsic water contact angle of air θ_{LV} is 180°, hence the simplification in equation 4 by eliminating components of the surrounding air [2, 4, 12].

It can therefore be deduced that, decreasing the area fraction of the solid material on the surface increases the static contact angle. This is achieved by fabricating highly rough surface protrusions to entrap adequate air to prevent wetting or create barrier between the droplet and micro-nano structures within the surface [2, 4], as demonstrated in Figure 3B. This results in low surface adhesion to the liquid droplet, and produces low contact angle hysteresis that can cause the droplet to roll at extremely low angles [2].

Therefore, superhydrophobicity can be achieved by increasing the surface roughness on the micro-nanoscale to decrease surface area fraction, and chemical functionalization to lower the surface energy to reduce the adhesive tendency between the solid-liquid interface [9, 13].

3 Superhydrophobic Surface Fabrication

This section discusses the creation of micro-nano hierarchical structures and modification of the surface chemistry to lower the surface energy.

3.1 Micro-Nano Hierarchical Surface Fabrication Methods

Fabrication of micro-nanoscale hierarchical structures on the surfaces of materials is an important technique of achieving superhydrophobicity [9, 13]. The choice of method for the fabrication of hierarchical structures for SHB surface is usually determined by the shape and type of material of the substrate. Fabrication methods such as atomic layer deposition and laser patterning [13], sol-gel processing and anionic oxidation that are used to fabricate micro-nano hierarchical structures on substrates [14]. This chapter discusses general methods used for fabrications on arbitrary shapes and materials.

3.1.1 Physical Vapor Deposition

Physical vapor deposition (PVD) is the atomistic deposition of vaporized material from solid or liquid source in atomic or molecular form and transported as vapor through vacuum or plasma environment on to a substrate to condense [15]. With a deposition rate of 1 – 10 nanometres per second, PVD can be used to deposit thin films with a few nanometres to micrometres in thickness to multi-layered coatings onto a substrate. The substrates applicable in PVD processes can be of different shapes from planar to complex geometries [14, 15]. The categories of PVD processes include vacuum deposition or evaporation, sputter deposition, ion plating and arc vapor deposition.

PVD method has been used to deposit thin film of n-hexatriacontane ($C_{36}H_{74}$) on a planar silicon wafer substrate as a process to achieving a superhydrophobic surface [14]. The n-hexatriacontane is a hydrophobic material which can form films with low surface energy of about 20 mJ/m^2.

SEM micrograph of the process as seen in Figure 4 shows the successful deposition of n-hexatriacontane on the silicon wafer. The surface texture appears randomly distributed clusters and varying nano – micro sizes of the deposited n-hexatriacontane.

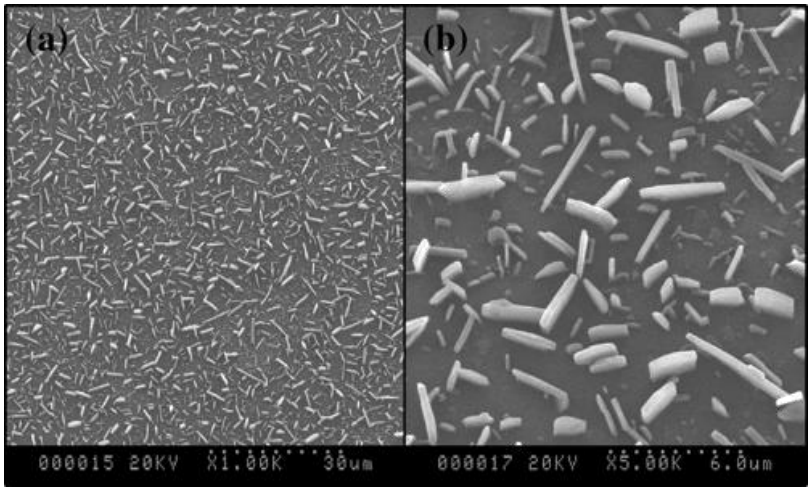

Figure 4: SEM micrographs with of deposited n-hexatriacontane on silicon wafer: (a) 1000X magnification and (b) 5000X magnification. The high magnification (b) clearly shows the randomness and varied sizes of the deposited material [14].

The wettability of the modified surface satisfied superhydrophobic features. The reported advancing contact angle was 170.9° and a receding contact angle of 165°. These results indicate that water droplet could not penetrate the spaces among the protrusions and the air pockets created by the deposited nano – micro sized low surface energy n-hexatriacontane particles on the surface of the wafer. Therefore, the fabricated layer satisfies the Cassie regime of wettability. [14].

Another category of PVD was adopted in depositing silver (Ag) nanoparticles polydimethylsiloxane (PDMS) substrate during the fabrication of superhydrophobic surface for antibacterial purposes [16]. This involved a thermal vapor deposition of Ag on to a carnauba wax-coated PDMS -paper surface in a vacuum chamber, as seen in Figure 5. The term PDMS-paper is used to refer to a textured surface of PDMS sheet with A4 print paper through replication. This replication introduced micro-channels

on the PDMS surface, making the texture of the PDMS surface appear like that of an A4 print paper. The prepared planar PDMS substrate was fixed in the vacuum chamber and rotated at 10 rpm while particles of Ag were evaporated from a target material of Ag.

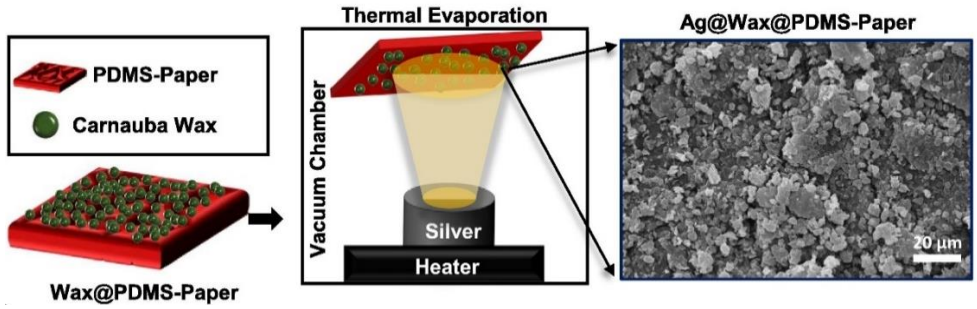

Figure 5: Thermal vapor deposition of Ag particles on to a carnaubau wax coated PDMS paper. From left to right: the depiction of the waxed PDMS-paper: thermal evaporation of the silver pellet within a vacuum chamber of the deposition tool and a SEM micrograph with scale 20 µm SHB owing the grains or nanoparticles of the deposited Ag particles [16].

The characterization of the fabricated surface indicated a superhydrophobic surface as seen in Figure 6, where water contact angle measured 169°, and selected liquids showed contact angle readings of over 150°. This is attributed to the low surface energy presented by the carnauba wax and the trapped air pockets presented by the thin layer of the deposited Ag. Thus, a successful fabrication of superhydrophobic surface [16].

Figure 6: Contact angle characterization of the fabricated surface. Droplets of selected liquids bead up to indicate superhydrophobicity, and the water contact angle indicated as 169° [16].

3.1.2 Laser Ablation

Laser ablation can be applied in vaporizing surfaces of hard materials like metals, ceramics and glasses [15, 17-20]. During laser radiation, some of the energy from the laser beam is absorbed by the surface of the target material, causing vaporization of materials [15]. Laser machining can be adapted to change the shape and surface properties of materials at the micro-nano scale. The physical properties of fabricated materials are directly influenced by the laser parameters and sample conditioning [17].

Laser beam can vaporize nanoparticles from target materials to be deposited on a transparent substrate in an arrangement where the laser beam for the irradiation is from the backside of the transparent substrate, as demonstrated in Figure 7 [21]. It can be observed from Figure 7 that the SiO_2 substrate is in proximity with the target gold material, and the femtosecond laser beam is passed through the transparent planar SiO_2 substrate on to the planar gold target. This is done in argon at atmospheric pressure, and can be applied to deposit thin films of nanometals on other optically absorbing materials including metals and semiconductors with the need for vacuum chamber [21].

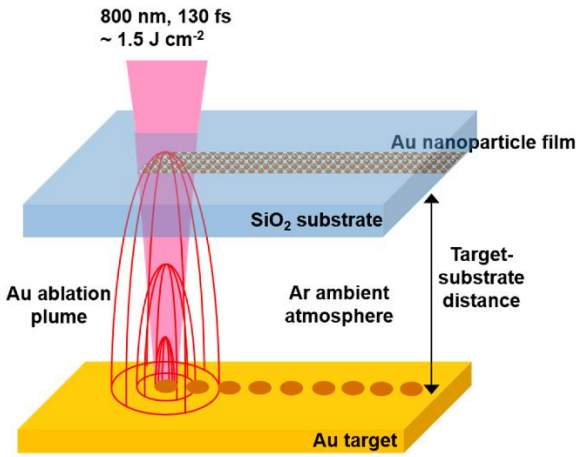

Figure 7: Deposition of thin film of gold nanoparticles on a transparent SiO_2 substrate with laser ablation. The laser beam is passed through the transparent substrate to vaporize the nanogold particles from the gold target. Image from [21].

Cardoso et al. [17] created superhydrophobic aluminium alloy surface by fabricating hierarchical structures with direct laser writing and laser interference pattering. This was achieved by using ultra-violet (UV) nanosecond laser system to fabricate square patterned microcell structures through direct laser writing. This was done with laser spot diameter of 15 µm, 355 nm wavelength in the ultraviolet spectra, fixed pulse duration of 30 ns, at a scan speed of 80 mm/s, at a repetition rate of 100 kHz and average laser power in the range of 170 – 490 mW among others. This was followed by using infrared picosecond laser to further divide the patterned microcells into sub-micron particles. This was done with an infrared laser source with pulse duration of 10 ps, interference area diameter of 160 µm,1064 nm of wavelength, repetition rate of 1 kHz, 89 – 293 mW of average laser power and scan speed of 1.6 – 68.8 mm/s. Superhydrophobicity was achieved with static contact angle reading of about 161° [17]. This SHB wetting feature is attributed to the trapped air pockets within the fabricated hierarchical structures.

Another method of using laser patterning on surfaces as demonstrated by Vanithakumari et al., [19] is the melting, vaporization, and re-solidification of hierarchical micro-nano structures on the surface of a titanium metal as part of a process of fabricating superhydrophobic titanium surface. Line

spacing was used as part of the patterning to determine the size of the ridges and grooves or the aggregated particles. Other relevant parameters included beam spot diameter of 50 μm, pulse width of 40 ns, scan speed of 120 mm/s, repetition rate of 10 kHz and average power of 10 W among others [19]. The stages occasioned by the ultrafast laser irradiation in the formation of the structures included the formation of multiscale precursor sites, followed by the organization of precursors into bigger structures and then their growth. This was dependent on the intensity of the laser spot and pulse repetition rate [17, 19].

Characterization of the surface topography indicated the patterned formation of hierarchical structures along the ridges created by the individual line spacings, as depicted in Figure 8. The sizes of the periodically arranged islands of the aggregated particles are dependent on the size of the line spacing adapted. Within the grooves are randomly distributed hierarchical particles in the micro – nanometre range which trap air pockets to facilitate superhydrophobic wetting features on the surface [19].

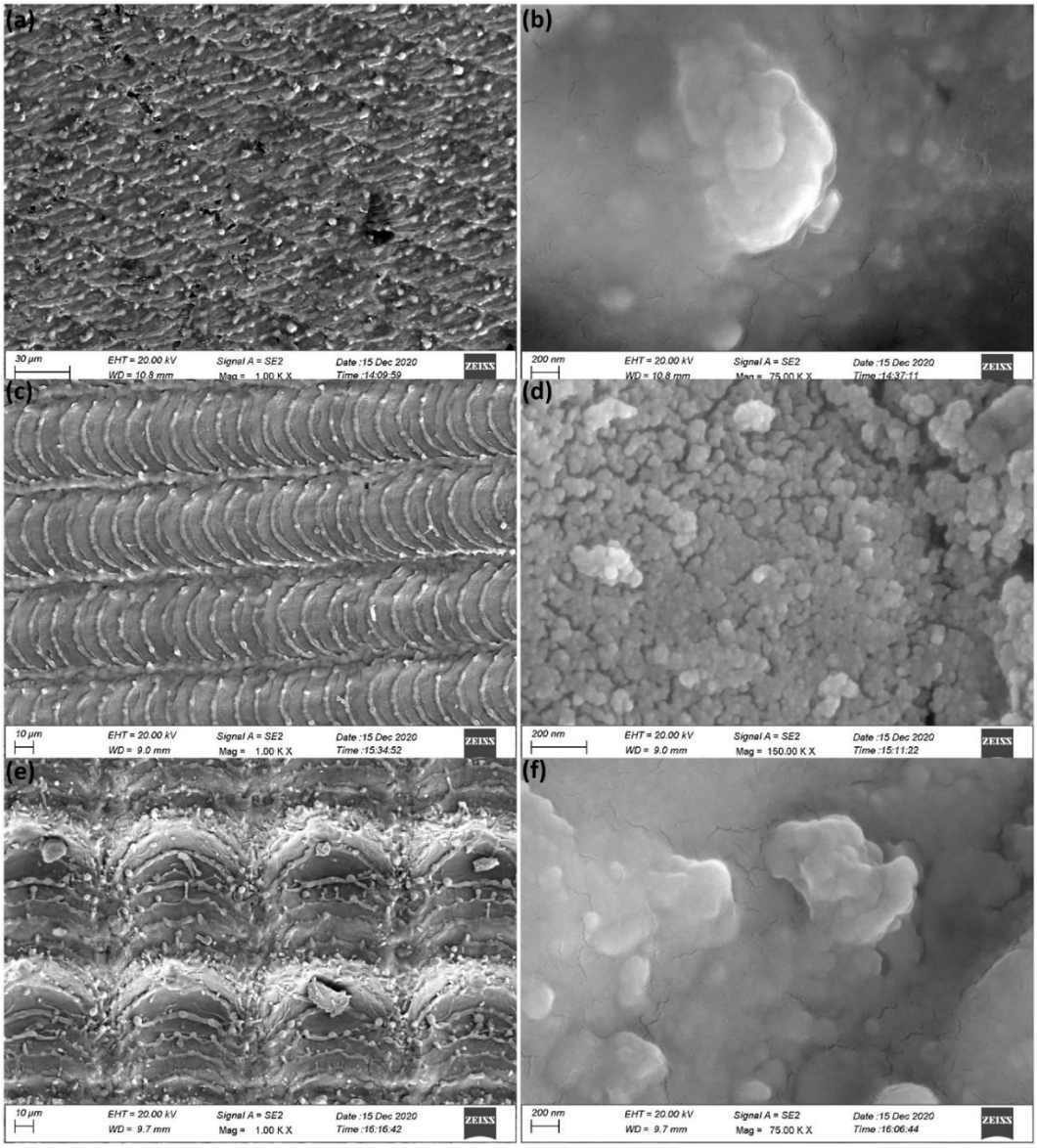

Figure 8: Field Emission Scanning Electron Microscope (FESEM) images of 3 of the line spacing parameters SHB owing low (left) and high (right) magnifications of the laser patterned titanium surface. Line spacing 20 µm are (a) and (b),50 µm are (c) and (d) and 80 µm are represented by (e) and (f). It could be observed from the left images that the periodically arranged grooves or aggregated particles sizes increase with increasing line spacing. The right images show the randomly distributed particles in the micro-nanometer range which create the conditions for superhydrophobicity. Image from [19].

As depicted in Figure 9, the wetting characterization even after 5 months of aging showed an average static contact angle of over 160°, while the untreated titanium surface produced a contact angle of about 55°. The micro – nanostructured particles within the grooves provided enough ground for

superhydrophobicity by trapping air within the micro – nano pores in between them to prevent wetting the surface, a form of double re-entrant geometry [8, 17, 19]. Also, the inherent stability and hardness of the base titanium material provided some robustness of the laser fabricated superhydrophobic surface, as evident in its positive results after aging.

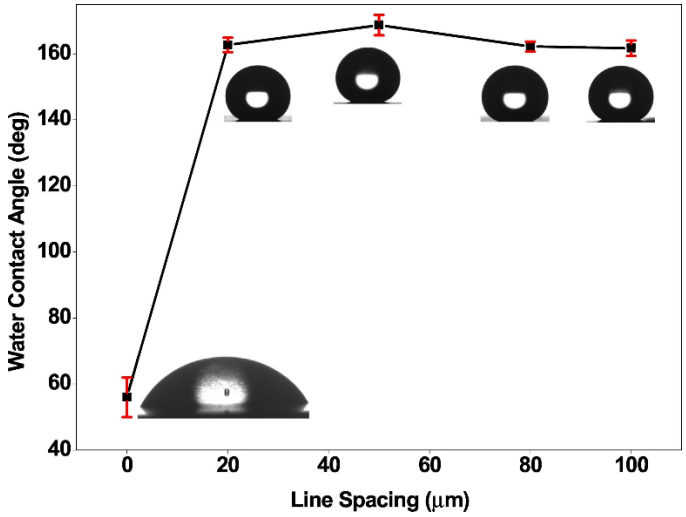

Figure 9: The static water contact angle for the four line-spacing laser patterned surfaces was about 160˚, while the untreated control surface produced about 55˚ [19].

3.1.3 Electrochemical Machining

Electrochemical machining is a process that enables the anodic dissolution of metal at low potential difference [22]. Aqueous solution of neutral salt, sodium chloride (NaCl), is usually the electrolyte of choice in this process [22, 23]. In this process, oxidation reaction between the metal and electrolyte leads to the dissolution of metal ions in the electrolyte solution. These ions then react with OH- and Cl- to facilitate precipitation of metal hydroxides and chlorides at the electrochemical cell. This process can be adopted to fabricate micro-nano pores and protrusions or hierarchical

structures on metallic substrates as a process of producing superhydrophobic surface.

In the first step of producing superhydrophobic Al surface by Song and co-workers [23], hierarchical micro-nano roughness as shown in Figure 10 were fabricated on aluminium Al surface through electrochemical machining or etching of the Al in $NaClO_3$ electrolyte.

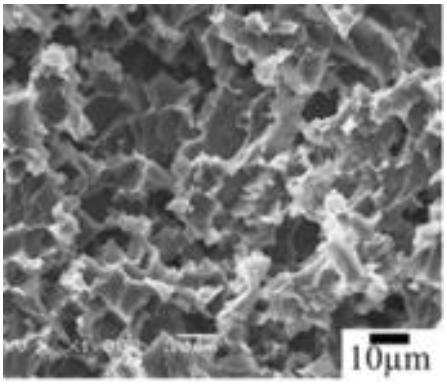

Figure 10: SEM micrograph of surface roughness on Al substrate produced by electrochemical machining. The resultant roughness serves as the first step in producing superhydrophobic Al surface [23].

The parameters of electrolyte concentration, processing times, and current densities were varied to ascertain their influence on the wettability or superhydrophobicity. The indications were that higher processing times resulted in higher contact angles as a lot more etching occurs; non-corroded areas decreased to increase roughness to produce higher contact angles when processing current density increases until homogenous rough structures are achieved. However, variations in the electrolyte concentrations show just little influence on the wettability. This is due to the flow of a constant current state as a result of the increase in processing voltage during decreasing electrolyte concentrations. [23].

3.2 Surface Chemical Functionalization for Superhydrophobicity

This section discusses some approaches to producing SHB wetting properties on surfaces pre-modified by introduction of micro-nano hierarchical structures.

3.2.1 Silanization

One method of fabricating an SHB surface is the design of micro-nano structured protrusions on a surface, and then introducing low surface energy materials to produce a surface with low surface energy [9, 20, 24, 25]. This section discusses some methods of introducing low surface energy materials to hierarchical surfaces, and a one-step fabrication for superhydrophobicity surface with just silanization [26].

Hydrophobic silane compounds have been used as functional agents to coat rough micro – nano hierarchical structured surfaces to achieve superhydrophobicity [20, 25]. They are usually alkyl silanes that lower the surface energy of surfaces. These compounds form compact and highly self-assembled monolayers (SAM) on hydroxyl-terminated materials surfaces such as silica, metal oxides and glass to modify the chemical functionalities of these surfaces [24].

Chemical modification of surfaces through silanization can be performed in a variety of ways. Some examples are discussed below:

Liquid-Phase Silanization

This phase of silanization involves the dispersion of the silane agent in a solvent. Two methods, dip coating and spray coating, have been used in this phase to achieve desirable superhydrophobicity on varied materials surfaces.

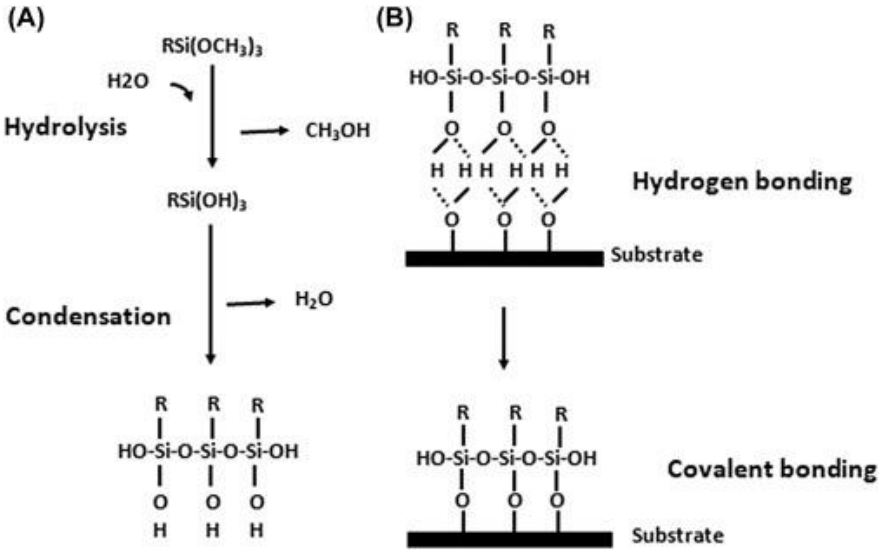

Figure 11: Chemical process for liquid-phase silanization reaction; (A) hydrolysis of alkoxysilane and condensation to form silanols, and (B) adsorption to the inorganic substrate by hydrogen bonding, and then covalent bonding through a condensation reaction with hydroxyl groups [27].

The initiation of silanization process within a solvent dispersion is the hydrolyzation of the alkoxysilane molecules. This leads to hydrolysis of alkoxysilane molecule in liquid phase (see Figure 11A), and then self-aggregation on the substrate or in the liquid, resulting in SAM formation [24, 26]. The resulting silanols coordinate with the inorganic surface hydroxyls by condensation reaction to form siloxane bonds to anchor the silane to the surface (see Figure 11B). An elevated temperature is then applied to stabilize the SAM by curing it to remove the remaining solvent and cross-linking adjacent silanols to form stable siloxane linkages [24, 27]. Zhang et al., [26] demonstrated the robustness of SAM for superhydrophobic coating on varied materials by proving its resistance to sand abrasion test.

Silanization by dipping substrates into solvent mixture of silane agents has been used to fabricate SHB surface. Nguyen et al., [20] functionalized a picosecond laser-textured hierarchical structures on a hydrophilic enamel structure into an SHB surface by dipping into fluorosilane agent. The textured enamel substrate was dipped into an ethanol solvent with one

percent by volume (1% v/v) concentration of perfluoroocytyl triethoxysilane (PFOTS) and left for 3 hours. This was followed by curing for 1 hour in temperature of 140°C. The resultant contact angle was about 180°, indicating that the silane agent successfully lowered the surface energy within the surface structures. Zhang et al., [26] also dipped or immersed a solid surface into a mixture with silane agent, octadecyl trichlorosilane (OTS), overnight to achieve superhydrophobicity with static contact angle over 168° and sliding angle less than 1°.

Spray coating is a popular means of functionalizing surfaces for chemical resistivity and superhydrophobicity [26]. Zhang et al., [26] have successfully used a one-step process to produce SHB surfaces by spray coating unmodified surfaces with silane agent. A mixture containing DI water, mineral spirit and OTS were thorough mixed and transferred into a plastic spray bottle and sprayed at 30° angle toward the substrate. The reported contact angle with 5 µL water droplet was greater than 170° and sliding angle less than 1°. This was attributed to the specialty of OTS in the presence of water, as it can be kinetically controlled to form micro – nano scale hierarchical siloxane aggregates on the surfaces.

Gas-Phase Silanization

A gas or vapor-phase silanization is another means of producing SAM of silane for superhydrophobicity. This method is better than its liquid-based counterpart because it has fewer sample preparation stages, it does not require potentially volatile organic solvents for dispersion and cost-effective as only smaller chemicals are required [28].

Prior to gas phase silanization, it is recommended to treat the substrates in oxygen plasma chamber to form hydroxyl (OH^-) groups on the surface. These groups form the platform for the silicon within the silane to form strong covalent R-Si-O bonds with, to attach themselves to the substrate [29]. The bonding between the low surface energy functional groups -CF_2

and -CF_3 together with silicon and the hierarchical micro – nano structures facilitate superhydrophobic conditions.

Gas or vapor-phase silanization has been used to fabricate SHB surface on titanium alloy substrate to serve antibacterial purposes [29]. In this instance, the surface modified titanium alloy was first treated in oxygen plasma, and then placed alongside a specific amount of heptadecafluoro-1,1,2,2-tetrahydrodecyl (trichlorosilane) on a hot plate in an enclosed chamber. The temperature was set at 120°C and left for 1 hour. The resultant contact angle was greater than 150° and roll-off angles less than 10°, satisfying the conditions for superhydrophobicity. Tasaltin et al., [28] also functionalized nano-porous and thin film alumina samples to become achieve superhydrophobicity, with a static contact angle of about 153°, via gas-phase silanization with hexamethyldisilazane (HDMS).

3.2.2 Polymerization

Polymerization is another means of functionalizing surface hierarchical structures to achieve superhydrophobicity. The micro-nano rough surface together with polymer coating reduces the surface energy of the solid surface to reduce adhesion between water droplet and the surface to enable Cassie-Baxter wetting regime [6, 30].

Monomers are the building blocks of polymers. The reaction which combines monomers to form polymers is polymerization [31]. Conversion of monomer to polymer via polymerization depends on the thermodynamic and kinetic consideration. A negative free-energy difference between the monomer and polymer, and adequate reaction conditions of initiation type and temperature must be satisfied to propagate polymerization [31]. Polymerization reaction can proceed in either step or chain reactions.

Step polymerizations involves the stepwise reaction between the functional groups of the reactants. The increase in size of the polymer molecule is at a slower pace as the process flow proceeds in the manner; monomer to dimer, trimer, tetramer, pentamer and so on. Reaction can occur between any of

these different-sized species present in the reaction system [31]. In chain polymerization however, an initiation is used to produce an initiator species with a reactive centre, which can be a free radical, anion or cation [31, 32]. This reactive centre is then propagated by the successive additions of monomer molecules in a chain reaction. Hence, in this type of polymerization, monomer does not react with monomer but with the reactive centre. [31].

Isakov et al. [6] functionalized a grass-like alumina layer with fluoropolymer via plasma-deposition of trifluoro-methane (CHF_3) to achieve superhydrophobicity. The fluoropolymer acted as the low-surface-energy to compliment the hierarchical structures of the grass-like alumina layer to produce SHB surface with advancing contact angle of 173° and receding contact angle of 160°.

4 Superhydrophobic Capillaries

Superhydrophobic coatings on the inner walls of tubes or capillaries or pipes have gained interest because of their ability to reduce drag to increase flow rate. This is because the SHB coatings introduce air cushion layer between the solid-liquid interface that prevents contact between the liquid and the solid surface [10, 33]. The complexity in geometry requires fabrication methods other than those of the highly researched planar geometry. The choice of the fabrication method for any capillary takes into consideration the length and diameter (aspect ratio) of the capillary to ensure effective coating. Some of the examples of the fabrication methods are discussed below.

4.1 Fabrication Methods of SHB Capillaries

4.1.1 Particle coating

Particle coating can be achieved by several methods including immersion and spray coating. The particles involved in this approach are usually dispersed in a solution, and the mixture introduced onto the surface of the material to form a coated layer [34]. The solvent is dried in appropriate conditions to leave the particles bonded onto the surface of the substrate. Figure 12 shows the FESEM micrographs of a SHB layer fabricated by spray coating the substrate. The coated particles agglomerate to create the desired hierarchical structures or micro-clusters with irregular voids and grooves to trap air [34]. The result was a static contact angle of 162°, sliding angle of 4° with 8 μL of water droplet and contact angle hysteresis <4° [34].

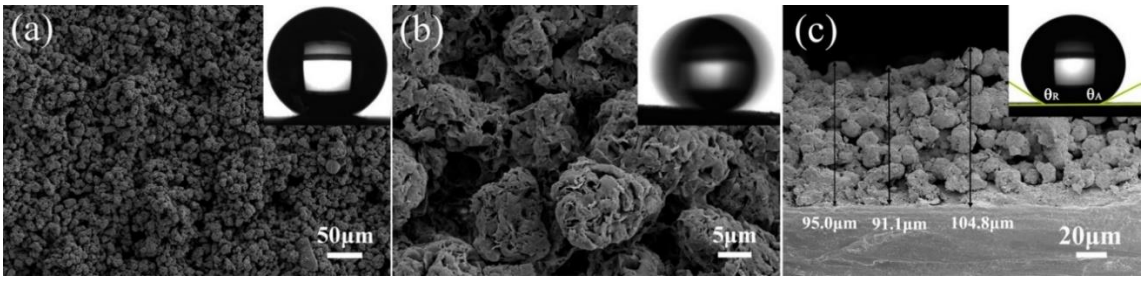

Figure 12: FE-SEM micrographs of superhydrophobic layer fabricated by spray coating and wetting features as insets: (a) low magnification with static contact angle of 162° (b) high magnification with sliding angle of 4° with 8 µL water droplet and (c) cross-sectional view of the agglomerated micro-nano particles with average thickness of 100 µm, and a contact angle hysteresis of <4° as inset. From [34].

This approach of hierarchical particle deposition is simple and cost efficient. It can also be used in arbitrary shapes and materials. Specifically, it has been used to create superhydrophobicity on the inner walls of glass tubes. Linear polyethyleneimine (LPEI) in aqueous solution was heated and sucked into a glass capillary to form a thin film layer, and the excess pushed out [9]. The glass capillary was then immersed in a solution containing an oligomer of tetramethyl orthosilicate (TMOS) at room temperature for a period. This caused the deposition of thin film of silica on the LPEI structured layer. This was followed by calcination at elevated temperature for a period to remove the organic component of LPEI layer. The silica nanograss was then functionalized by immersion in silane solution and allowed to dry. This resulted in a fabricated SHB surface with contact angle greater than 170° [9].

Vuckovac and co-workers [10] also fabricated a transparent superhydrophobic glass tube by dip coating. This involved the filling of 4.20 mm inner diameter capillaries with a drop of commercially available Hydrobead Standard with a pipette. The capillary was then dried with nitrogen flow and annealed at elevated temperature for a brief period. The resultant static contact angle was over 150°.

4.1.2 Replication

Using templates or molds as replicas to create hierarchical micro-nanostructures on surfaces can be employed to create SHB surfaces [33, 35]. The templates or molds can be made from metallic glass or metals such as nickel, steel, and aluminium[35]. The roughening of the replica can be done by several processes including etching and alkalizing [33]. Figure 13 outlines the processes involved in replication. Firstly, the Al mold which has the micro-nano hierarchical structures and micro – nano pores is created by chemical etching. This is followed by the introduction of the polymer or elastomer material on to the surface, to be heated to facilitate fluidity into the replica surface to produce the replication.

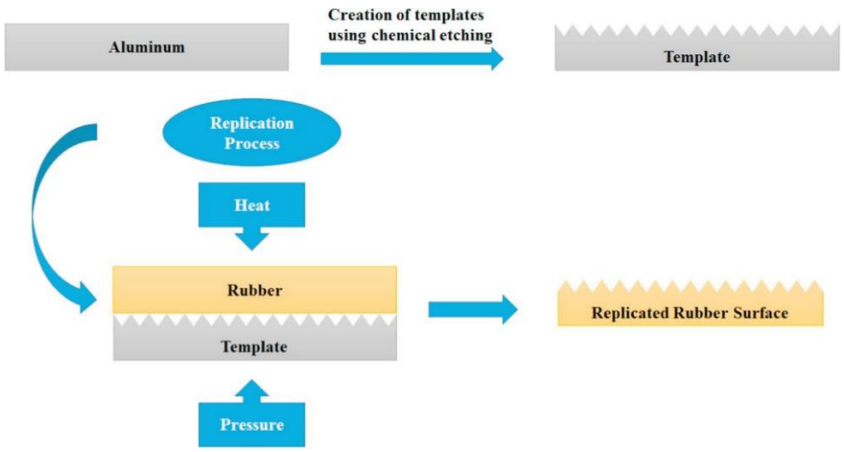

Figure 13: Replication fabrication steps. The process begins with the creation of micro-nano hierarchical structures on aluminium metal by etching. This is followed by the introduction of the rubber, being the material to be replicated, on the modified surface of the template. Heat is then applied to soften or melt the material to enhance fluidity into the grooves within the template to facilitate the replicating. Picture adopted from [35].

Kim et al., used replication method to fabricate superhydrophobicity on the inner walls of hydrophobic polydimethylsiloxane (PDMS). This was accomplished by just introducing hierarchical micro-nanostructures on the surface of the PDMS capillary. The inherent hydrophobicity and low surface energy of PDMS meant it required no surface treatment after the introduction of the hierarchical structures [33].

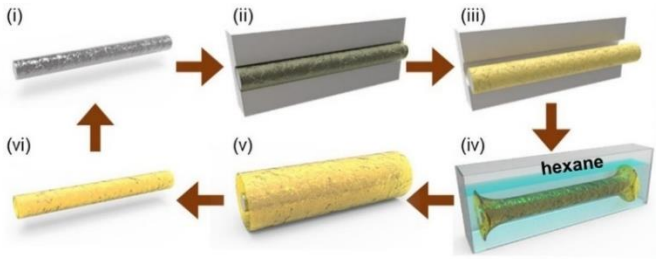

Figure 14: Replication process in producing a superhydrophobic tube: from (i)-(iii) indicates the surface modified aluminium rod placed in outer cases of the mold; (iv-vi) indicates the swelling mechanism adopted to separate the rod from the ready tube [33].

The fabrication process, as depicted in Figure 14 [33] involved the creation of the rough surface on aluminium rod template. Then, the PDMS was diluted in toluene to increase fluidity and then degassed in vacuum. The PDMS was then filled between the aluminium mold and the cylindrical outer cases and then cured under vacuum to remove air and facilitate adequate permeation within the hierarchical structures on the mold. Separation of the PDMS from the mold was achieved by swelling the PDMS to cause detachment while preserving the integrity of the template in the n-hexane solution.

The result was the development of hierarchical structures on the inner walls of PDMS tube as shown in SEM micrographs in Figure 15. The inner walls of the tube replicated the micro-nano hierarchical structures on the Al replica. The tube exhibited anti-wetting behavior with static contact angle of 155.5° and sliding angle of 8.4° with droplet volume of 20 μL [33].

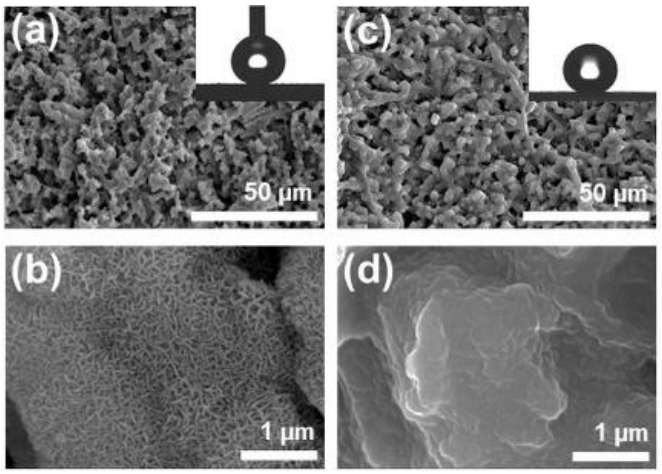

Figure 15: SEM micrographs showing the surface morphologies of the Al replica mold (a) and (b), and the replicated PDMS tube (c) and (d). Contact angle measurements inputs in (a) for the Al mold and (c) for the replicated tube. The rough surfaces modified on the Al mold was replicated or mimic on the inner walls of the PDMS tube. From [33].

The replication fabrication approach is simple and time and cost efficient and can therefore be scaled for bulk production [35]. The fabrication approach by Kim et al., [33] also provides control parameters to fabricate high aspect ratio tubes. High aspect ratio tubes can be fabricated by adjusting the aspect ratio of the mold, and the tube's thickness can also be varied by adjusting the space between the mold and outer cases. However, it is mostly limited to soft materials like polymers and elastomers [35] because a lot of energy would be required to melt hard materials such as glass and metals for their fluidity to effectively replicate micro-nanostructures on them.

4.1.3 Electroplating

Electroplating technique is used to deposit hierarchical structures on surfaces, to be functionalized or modified by low surface energy treatment to achieve superhydrophobicity [36, 37]. Deposition by electroplating involves oxidation and reduction processes. As seen in Figure 16A, oxidation reaction occurs on the nickel electrode to cause the dissolution of nickel ions Ni^{2+} in the electrolyte, while the reduction process involves the

deposition of the dissolved nickel ions from the electrolyte onto the mild steel rod serving as the cathode electrode [38].

This process can be controlled to produce an exact thickness layer, for a well-defined, high-quality surface with a conformal thickness profile. Different waveforms through variations in applied current can be used to influence the microstructure, multilayers, and composition of the coating. The current flowing through the cell is determined by the rate of reduction of metal ions, and the overall charge is proportional to the overall coating mass and thickness. [38]. Hydrogen evolution reaction which produces gaseous hydrogen facilitates the introduction of impurities or imperfections in the coating, can be prevented by applying the adequate current density [37]. Large overpotential can cause the emission of a lot of hydrogen which can affect the morphology of the deposition [39].

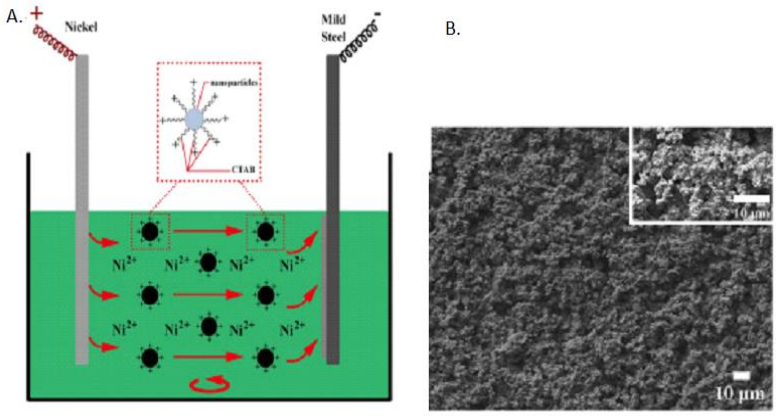

Figure 16: Electroplating method for introducing hierarchical roughness on the surface of capillaries: (A) an electrochemical cell setup for the electroplating of mild steel surface with nickel. The nickel metal dissolves into ions of Ni^{2+} in the electrolyte and are transported to coat the mild steel because of potential difference across the electrodes, and (B) SEM micrograph of the resultant hierarchical structures of nickel coated on the surface of the mild steel [37].

The resulting hierarchical structures, depicted in Figure 16B can be fabricated on a variety of materials and shapes. The surface chemistry of the deposited particles was modified by introducing stearic acid self-assembled

monolayer to reduce the surface energy to create superhydrophobicity, with a static contact angle of about 170°.

Electroplating or electrodeposition can be used to apply hierarchical coatings on complex shapes including the inside surface of pipes [40]. This is demonstrated by Asiabi and co-workers [41] by electroplating the inner surface of stainless-steel tube of 0.75 mm diameter with nanostructured polyaniline-polypyrrole composite. Ling and Torii also electroplated the inner walls of 10 mm stainless steel pipe with porous copper structure [39]. In [39], the fabrication process involved a variation in the overpotential and time to influence sizes of the deposited copper particles depicted in Figure 17. Higher overpotential over longer periods caused hydrogen evolution which triggered nucleation to achieve bigger and deeper microporous copper deposits. In contrast, lower overpotential over short periods resulted in deposition of smaller particles to create thin copper layer.

Although the application of the deposited microporous copper particles on the steel pipe was heat transfer enhancement purpose, the successful deposition of such microporous metal on a surface can be functionalized by silanization or polymerization and others to achieve superhydrophobicity [9, 20, 24, 25].

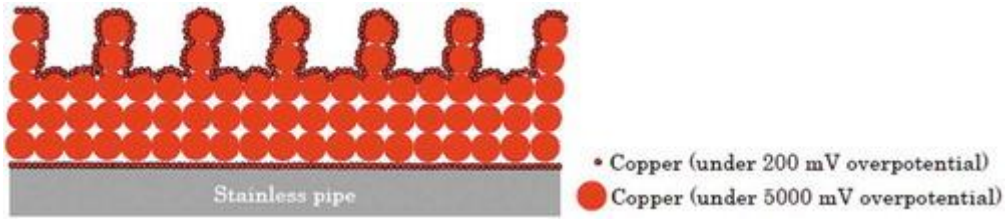

Figure 17: Schematic of microporous copper electroplating of the inner surface of pipe. Variations of overpotential and time are used as control mechanisms to deposit different sizes of microporous copper particles on the inner pipe surface [39].

4.1.4 Atomic Layer Deposition

Atomic layer deposition (ALD) is a self-limiting deposition technique of that permits homogeneous, conformal thin film deposition with nanoscale thickness control. It is used to fill high aspect ratio surface features and porous materials [15, 42, 43]. ALD differs from chemical vapor deposition (CVD), because CVD involves a simultaneous presence and reaction of the precursors during deposition, while in ALD processes, there is a sequential exposure of the different precursors or reactants to the substrate during deposition [42, 43].

In the 1960s, Aleskovski and co-workers carried out a Molecular Layering which was the first work with the semblance of the now ALD. The technology was further developed in the 1970s by Suntola and co-workers and renamed Atomic Layer Epitaxy (ALE) [42, 43]. But the concept of epitaxy, which is the single crystalline growth on a crystalline substrate, was limited in his work, therefore, ALD was adopted as the general name.

An ideal ALD growth cycle is characterized are exposure of substrate surface to first precursor; chemisorption of the first precursor onto the substrate; a purging step with an inert gas; introduction of second precursor; surface reaction to produce thin film and inert gas purge to remove gaseous reaction by-products [43]. All these stages occur within certain temperature window to deposit the desired film thickness within a certain period. This temperature window must not be too high to decompose the precursors or too low to absorb more than one monolayer per cycle or condense impurities on to the substrate surface [42].

The growth rate of ALD deposition is usually one monolayer per cycle, but in some cases the deposition rate is less than a monolayer. This can because the second precursor does not provide enough atoms to react with all the element of the layered first reactant for a product film [42].

ALD coating has provided a means to deposit thin films on arbitrary shapes of different materials. Isakov et al., [6] deposited alumina (Al_2O_3) on planar soda lime glass wafers with ALD as a process in fabricating a SHB antireflective surface. Xiao et al., [44] fabricated an SHB wool fabric by

introducing Al_2O_3 nanoparticles on the surface of the wool fibre by ALD coating of Al_2O_3 at 80°C for 100 cycles.

Also, Li et al., [45] fabricated a transparent SHB glass with ALD coating of aluminium doped zinc oxide (AZO) followed by hydrothermal treatment of the AZO layer to form micro-nanosized flowers, see Figure 18. The growth per cycle (GPC) of the ALD was about 1.5 Å/cycle. The hydrothermal treatment was done at an elevated temperature with a solution including a 1:1 ratio of zinc nitrate hexahydrate and hexamethylenetetramine (HMTA).

The HMTA degrades in the hot water to release hydroxyl ions, which react with Zn^{2+} ions to form zinc oxide (ZnO) nano hierarchical structures [46]. The HMTA could preferentially attach itself to the nonpolar (100) planes of the zincite crystal, which are stable with lower surface energy, to prevent access of Zn^{2+} ions to them, leaving only the polar (002) planes for epitaxial growth [45, 46].

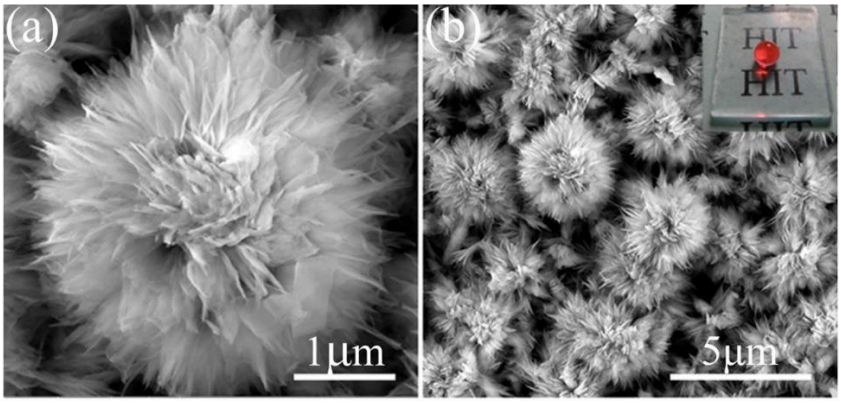

Figure 18: FE-SEM images of the fabricated AZO micro-nano flower through ALD deposition of AZO and hydrothermal treatment: (a) high magnification and (b) low magnification, with inset of a digital image of AZO- coated glass substrate with a droplet with static contact angle of 170° [45].

The fabrication results indicated that high concentrations of HMTA increase the nucleation rate of the AZO crystal grains. However, the optical transmittance is decreased at high concentrations of HMTA. At an optimal concentration of HMTA, the fabricated hierarchical peony-like AZO surface

showed water contact angle of 170°, hence a successful fabrication of a SHB surface [45].

Li et al. [45] further proposed the possibility of using this fabrication method to produce SHB surfaces on inorganic oxide materials with complex shapes.

Zhu and co-workers [47] have demonstrated the possibility of depositing thin film of titanium dioxide TiO_2 on the inner walls of metallic tubes with ALD for anti-coking purposes. The average GPC was 1.1 -1.3 Å/cycle which agrees with GPC in literature [48]. Therefore, it can be deduced that the fabrication method adopted by Li et al. [45] can be applied on the inner walls of tubes for superhydrophobicity. A similar method of fabrication adopted in this Thesis work is to fabricate superhydrophobocity on the inner walls of glass tubes.

4.2 Fluidic Performance in Capillaries

This sub-chapter discusses the parameters used to measure the performance of fluids in pipes, capillaries or tubes to ascertain the relationship between the liquid-solid interface.

4.2.1 Frictional Factor and Reynolds Number

The evaluation of frictional head losses in pipes, capillaries or tubes is a vital factor that greatly influences their design and fabrication to facilitate hydraulic balance of a flow network and enhance cost-efficient operation [49]. It has been reported that the roughness level of a tubular surface determines the flow behavior of fluids [10, 49-51].

SHB surface coatings reduces surface friction. The solid surface wall friction is substantially reduced by the layer of air-pockets within the micro-nanopores introduced within the hierarchical structures of the SHB layer (see Figure 19A) [51, 52]. This leads to a reduction of the solid surface area fraction, and thus reduced resistance between the fluid and the surface.

This condition introduces slip boundary conditions (see Figure 19) for moving fluid over the surface [53].

The weak adhesion force between water droplet over a SHB surface with high surface roughness and low surface energy implies that the cohesion force among the bulk water molecules is higher and tends to pull away from surface, as demonstration in Figure 19B. This leads to the depletion of the water molecules in contact with solid surface (near-wall region in Figure 19B). The depleted water molecules become less viscous than the bulk liquid molecules. The tendency for the liquid droplet to stay in equilibrium causes the liquid droplet to move or slip away from the surface [54]. Slip length and slip velocity of flowing fluid over SHB surfaces lead to an increase in fluid flow rate [51]. Yan and co-workers [51] have demonstrated that the frictional factor of a SHB capillary surface can be reduced by up to 35%.

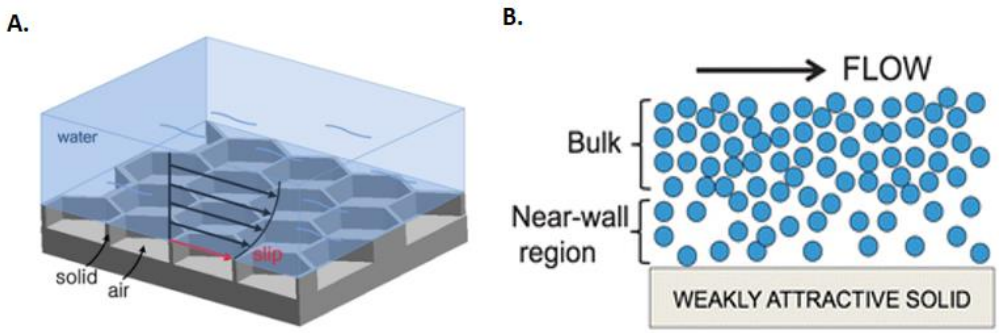

Figure 19: Demonstration of liquid droplet slippage over SHB surface with reduced frictional factor: (A) Water droplet slippage over a SHB surface with low surface energy as a result of reduced solid surface fraction to increase air pocket and low surface energy modification [53]. (B) Simulation with droplet molecules over a SHB surface with low surface energy. The cohesive force among the bulk liquid molecules remains higher than the adhesion force of the solid surface and the Near-wall region of the liquid droplet, hence, the higher cohesive force draws the bulk droplet away from the surface [54].

Reynolds number is a dimensionless number used to classify the type of liquid flow in capillaries [51], as expressed in equation 5. A flow of liquid in capillaries can be in layers of lamination without turbulence, which is termed as laminar flow. However, increase in the liquid flow rate leads to

increased flow velocity, which could lead to a turbulent flow with disturbances, which is also known as turbulent flow [51, 55].

$$Re = \frac{Dv\rho}{\mu} \quad 5$$

From equation 5, D is the tube diameter, v is the average flow velocity, ρ is density of the fluid and μ is the fluid viscosity [53]. The flow of fluids in pipe is categorised as laminar flow if the value of the Reynolds number is smaller than the critical Reynolds number of 2300. The flow is in transitional region between Reynolds numbers 2300 and 4000 [50]. After Reynolds number 4000, the flow is categorised as turbulent [49, 50].

According to Yan and co-workers [51], there exists a relation between Reynolds number which is used for flow classification, frictional factor and slip length. This is expressed in the equation 6 below:

$$\frac{1}{f} = \frac{Re}{64}\left(1 + \frac{8b}{D}\right) \quad 6$$

Frictional factor is represented as *f*, *Re* is the Reynolds number, *b* is the slip length and *D* is the inner diameter of the capillary. Reynolds number for fluidic flow in capillaries is also expressed as:

Fluidic pressure or hydrostatic pressure because of the force of gravity exist on the surface of water in reservoir, which is proportional to the height of the water. The flow of fluid in a capillary is due to a hydrostatic force which a depends on the local hydrostatic pressure and the cross-sectional area of the capillary in the relation in equation 7 [56].

$$H_f = H_p A_c = \ \rho g h \times \pi r^2 \quad 7$$

From the above equation, H_f is hydrostatic force, H_p is hydrostatic pressure and A_c is the cross-sectional area of the glass capillary; ρ is density of the

fluid, *g* is acceleration due to gravity, *h* is the water height and *r* is the radius of the capillary.

4.2.2 Drag Reduction and Sliding Angle

Drag reduction or reduction of hydraulic resistance is achieved as a result of hydrodynamic sliding of liquid over superhydrophobic surface [57]. The micro-nano hierarchical structures and the double re-entrant structures fabricated on surfaces for superhydrophobicity provide adequate surface roughness and micro-nanopores for air entrapment to facilitate shear-free, air-liquid interface for contact line-free, continuous liquid flow [58]. Such SHB surface as depicted in Figure 20 provide trapped air in the micropores to prevent wetting between the peaks of the rough surface, just as in the Cassie state of wetting, which is fully dry surface [58, 59]. This result in slip-induced drag reduction flow of the fluid in the tube or capillary.

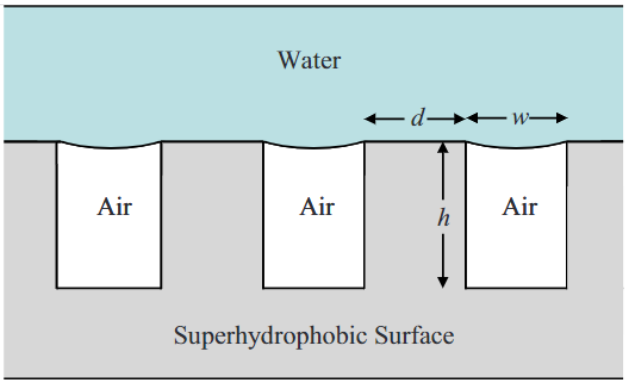

Figure 20: Schematic of rough solid surface with trapped air between the peaks for non-wetting and slip-flow purposes. The dimensions d, w, and h are in micro-nano range. Such micro-nanopores occasioned by the hierarchical structures provide room for air to be trapped to facilitate Cassie wetting regime, helps to produce slip leading to reduction in drag force on the flowing water [58].

The magnitude of drag reduction is dependent on the size of the microtextured surface, function of geometry and Reynolds number. Hydrostatic or hydrodynamic pressure can adversely influence the drag

reduction capacity of a surface. Cassie state of wetting, which is the required wetting model to achieve drag reduction, can be transformed into Wenzel state of wetting when there is high pressure on the surface. The high pressure would cause the liquid to penetrate the micropores between the beaks to cause wetting. Also, regular pattern of roughness creation other than random roughness leads to higher magnitude of drag reduction [59].

Low surface energy of SHB surface contribute to reduction of hydraulic resistance. It has been exhibited that the sliding of the liquid molecules over SHB surface is possible because of the superiority of cohesion force between the liquid molecules relative to the adhesion force between the solid-liquid interface [57].

Reducing drag in fluid flow can lead to reduction in pressure drop in pipeline systems because flow rate is increased with drag reduction at constant pressure [59]. It also improves fuel efficiency and higher speed capabilities of marine vessels [58, 59]. Also, from the Reynolds number equation at equation 5 above, reducing drag in capillary flow is a means for increasing Reynolds number in both laminar and turbulent flows. This is because v, which is the average flow velocity can be increased with reduced drag [57], hence an increase in Reynolds number [58]. It has also been demonstrated that, at low Reynolds number, higher drag reduction can be achieved [7, 60]. Hoshian and co-workers [7] achieved up to 68% drag reduction with a 2 mm SHB tubes and 38% with 4 mm SHB tubes at low Reynolds numbers.

Fluid droplet can move by sliding or rolling on a tilted surface. A change in shape of the spherical droplet can be necessary before it begins to move. This shape change of droplet is regarded as an activation barrier to motion. This activation barrier is quantified by the increase in liquid-vapor interface area considering the solid-liquid contact area remains constant, and expressed as [11]:

$$E_a = \gamma_{LV} \times \Delta A_{LV} \qquad 8$$

Where E_a is the activation barrier, γ_{LV} is the surface tension at the liquid-vapor interface and ΔA_{LV} is change in liquid-vapor interface area. However, if the solid-liquid contact area changes due to a change in the spherical shape of the droplet before motion, then the activation energy is the summation of the individual activation barriers of the three interfaces expressed as [11]:

$$E_a = \gamma_{LV}\,\Delta A_{LV} + \gamma_{SL}\Delta A_{SL} + \gamma_{SV}\Delta A_{SV} \qquad 9$$

From the equation above, E_a is the activation energy, γ is surface tension, ΔA is change in area, LV is liquid-vapor interface, SL is solid-liquid interface and SV is solid-vapor interface. Therefore, SHB surfaces with extremely low CA hysteresis have low activation barrier to overcome as there is minimum change in shape of the droplet to cause it to move. On the contrary, droplet on hydrophilic surfaces must overcome higher activation energy to move as such activation energy includes the sum of the activation barriers of the three interfaces of solid-liquid-vapor as expressed in equation 9. [11].

The driving force of water droplet in a capillary is influenced by the wettability, which include the advancing and receding angles and CA hysteresis, of the surface along the capillary and the inner radius [61]. This relation is expressed in the equation below [7, 61].

$$F_{dr} = 2\pi r\gamma(cos\theta_{adv} - cos\theta_{rec}) \qquad 10$$

Where F_{dr} is the driving force, r is the radius of the capillary, γ is the surface tension of sliding droplet, θ_{adv} is the advancing CA and θ_{rec} is the receding CA. Consequently, the bigger the diameter of a capillary the bigger the driving force of the liquid droplet, considering all other variables are constant [61].

5 Materials and Methods

5.1 Tubes and Reference Materials

Three different diameters of 500 mm long borosilicate glass tubes were sourced from Fischer Labortechnik via Avantor and VWR Finland [62]. The tubes are 6 mm inner diameter (ID) with 1 mm wall thickness (WT), 4 mm ID with 1 mm WT and 0.6 mm ID with 0.7 mm WT. Borosilicate glasses were chosen due to their excellent chemical and thermal resistance. These properties ensured the physical and chemical integrity of the tube would be maintained during ALD deposition at elevated temperatures.

The tubes were cut into the length of 100 mm. The sharp edges were thoroughly filled with sandpaper. The tubes were then cleaned with ultrasonic cleaner in isopropanol for about 1 hour.

Planar silicon with dimensions between 10 – 20 mm were used as flat references and they underwent the fabrication steps simultaneously with the capillaries. This was to provide a planar surface for efficient examination of the coated films. Specifically, the measure of fluidic performance such as contact angle measurement with a goniometer and the layer thickness measurement with ellipsometer require a planar surface. It is assumed that the ALD growth conditions and hydrothermal treatment on both substrate materials and shapes under the same parameters should yield same thickness and particle structure.

5.2 Superhydrophobic Surface Fabrication

This fabrication approach is a modified version of the Al_2O_3 nanograss fabrication process by Kauppinen et al. [63] applied to capillary instead of a planar surface. The fabrication process flow follows the chart depicted in Figure 21. Each of the steps in the process flow is discussed further in the next sections.

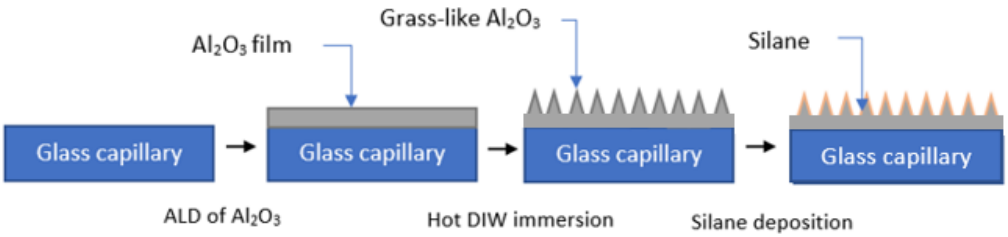

Figure 21: Process flow chart of the fabrication method adopted in this Thesis. The fabrication begins with preparing the capillaries, which involved cutting and ultrasonic cleaning. The next step was ALD deposition of alumina film on the inner walls of the capillary. This was followed by hot water immersion (hydrothermal treatment) at 85 – 90 C for 30 minutes to grow the alumina film into micro-nano grass-like structures. The final step was the SAM treatment to introduce a layer of silane on to the surface. Prior to the SAM treatment was oxygen plasma treatment. This process flow chart is an edited version from [6].

5.2.1 Atomic Layer Deposition (ALD)

The first step in the fabrication process flow is the ALD of Al_2O_3 to achieve a conformal thin film on the inner walls of the tubes. The ALD tool used is a Beneq TFS-500 reactor. The size limitations of the ALD sample holder influenced the fabrication of the samples in smaller batches. Each batch had at least one of each different diameter of capillaries and two monitor planar Si wafers – one at each end of the capillaries (inlet and outlet) in the ALD sample holder.

The process used is described in detail by Kauppinen and co-workers [63]. It involves ALD processing at 120°C at 5 mbar and run for 340 cycles with trimethylaluminum (TMA) and water as precursors. The number of cycles was increased from the 313 cycles used by Kauppinen and co-workers [63] to achieve similar film thickness. This was because the average GPC achieved from the fibre reactor used here was smaller (0.77 Å) compared to the larger GPC (0.83 Å) achieved with the reactor used in [63]. The pulse times for both TMA and water were 200 ms, while the purge times were

also different from the reference process [63]. The carrier gas was nitrogen, which flowed at 200 sccm.

5.2.2 Hydrothermal Treatment

The second step was the immersion of the ALD coated tubes and wafers into a beaker of heated deionized water (DIW) at 85 – 90°C for 30 minutes. The beaker was an IKA HBR 4 digital heat bath with built-in temperature control. This step facilitated the growth or transformation of the as-deposited Al_2O_3 film into a porous, grass-like structure.

5.2.3 SAM Treatment

The surface functionalization begins with oxygen plasma treatment of the surfaces the samples in a Tepla 400. The recipe for this process was 60 W, 500 ml/ min of oxygen and 1 minute. The treatment introduced hydroxyl (OH^-) groups on the substrate surface. These groups once attached to the substrate, form the platform for the Si-Cl group in the SAM chemical to form strong covalent R-Si-O bonds with.

The gas phase silanization immediate followed oxygen plasma treatment. This was done with 35 µg of powdered 1H, 1H, 2H, 2H-Perfluorododecyltrichlorosilane ($CF_3(CF_2)_9CH_2CH_2SiCl_3$) sourced from Sigma Aldrich [64]. The measured silane sample was placed in a small high temperature petri glass and placed in a bigger high temperature petri glass together with the ALD coated tubes and monitor silicon wafer samples. The bigger petri dish was then covered with its lid and placed on an 80°C hot plate and heated for 2 hours. This gas phase silanization was done in a closed petri but otherwise under ambient pressure and humidity.

5.3 Surface Characterization

5.3.1 Ellipsometry

Ellipsometry was done to determine the thickness of the and uniformity of the coated layer over the different sample batches. Micronova Cleanroom's Plasmos He–Ne ellipsometer working at 633 nm wavelength was used for this purpose.

The two monitor planar Si wafers that were coated simultaneously with the glass tubes in each batch were used for this characterization. It is assumed that if both planar monitor samples show similar film thicknesses, then the film thickness on the inner walls of the capillaries is average of the thicknesses from both monitor samples.

5.3.2 Scanning Electron Microscopy

Scanning Electron Microscopy (SEM) was done to ascertain the success of the fabrication processes in coating the different tube diameters and analysis the features of the coated layer. The SEM EBL Zeiss Sura 40 was used for this purpose. The 100 mm long capillaries were divided into five sections, in 20 mm long sections. The first 20 mm at one end and the third 20 mm from the middle sections of each capillary were analyzed with SEM.

One of the ends of the capillaries was used because both ends have the same exposure level in the ALD and hydrothermal systems. The middle section is farthest from both ends, and thus, the best location to provide the most varied features of the fabricated Al_2O_3 layer if any. The SEM analysis of these sections of the capillaries to determine the success of the ALD and hydrothermal treatment fabrication in terms of the aspect ratio of the capillaries.

Pieces of glass from each section were cut out, cleaned and sputtered with 11 nm thick gold film. The gold film helps to introduce electrical conductivity to the glass to reduce charge accumulation.

5.3.3 Contact Angle (CA) Goniometry

The advancing and receding CA measurement were done with a Contact Angle Meter THETA to evaluate the wetting behavior of the fabricated SHB layer. Again, the planar silicon wafer was used for this purpose. Three random spots across the wafer were measured for an average CA. The advancing CA measurement was done with 18 MΩ-cm deionized water (DIW) droplet from 2 μL to 5 μL, while the receding CA was from 5 μL to 2 μL at a flow rate of 0.1 μL/s.

5.4 Fluidic Characterization

The fluidic performance of the coated tube is assessed in this section. Different fluidic experiments were performed and are discussed below. All experiments were performed with both SHB capillaries and corresponding as received capillaries serving as controls. For the purpose of this set of experiments, 25 mm long ID-0.6 mm capillaries were fabricated to achieved SHB coating on the total inner surface area. Four of such capillaries were carefully joined together to get 100 mm long ID-0.6 SHB capillaries.

5.4.1 Droplet Sliding Angle

The sliding angle of the surface of the inner walls of the glass tubes were evaluated with tilting stage, as demonstrated in Figure 22 with the ID-6 mm SHB capillary. The glass tube was fixed on a tilting stage at 0° (Figure 22A) and a measured amount of deionized water (DIW) droplets were placed into the SHB and control glass capillaries (both 100 mm long) with pipette. The volume of droplets was calculated so that the length it covered in each of the tube diameters was the same, and the droplet was large enough to touch the entire circumference of the tube. This was to standardize the measurements. The droplet volumes were 500 μL for ID-6, 200 μL for ID-4 and 35 μL for ID-0.6. The stage was then slightly tilted (Figure 22B and C) until either part of the water droplet or the whole droplet slide out (Figure

22D) of the capillary. The experiment was performed three times with each capillary, and the reported values are averages of these plus-minus standard deviation.

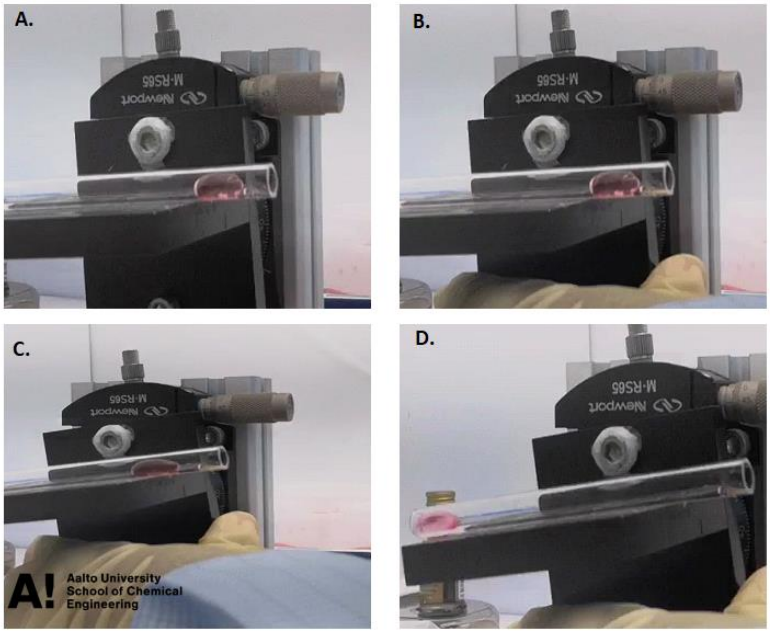

Figure 22: Water droplet sliding angle measurement: (A) water droplet in a SHB capillary at 0°, (B) water droplet in SHB capillary at the beginning of tilting, (C) water droplet begins to slide (D) Water droplet just slides out of the SHB capillary.

The bio-repellency capability of the SHB coating was also analyzed. This was done by examining the sliding angles of droplet of the protein solution of bovine serum albumin (BSA) sourced from Fisher Scientific Finland [65]. Three different concentrations of 2 µg/ml, 20 µg/ml and 200 µg/ml of BSA were prepared by dissolution in phosphate-buffered saline (PBS) buffer, which is also sourced from Fisher Scientific Finland.

5.4.2 Hydraulic Drag Resistance

This was done to evaluate the friction reduction and thus, the improved flow velocity in the SHB tubes as compared to the control tube. The setup for this experiment followed an experimental setup by Kim et al. [53]. A

schematic illustration is presented in Figure 23 below. Hydrostatic pressure acts on the water surface in the reservoir, and it is proportional to the water height, which is from the water surface to the exit hole where the capillaries are insert on the beaker [53] as shown in Figure 23.

.

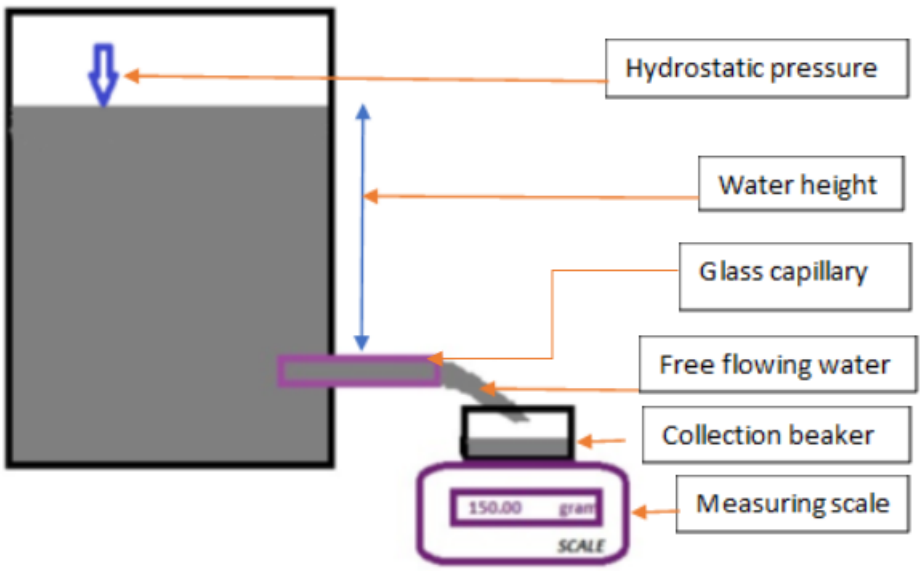

Figure 23: The experimental setup for drag reduction evaluation. This setup is adopted from [53].

The evaluation was done with different water heights with 50% step reductions (68. 5 cm, 34.0 cm and 17.0 cm) to evaluate the effects of hydrostatic pressure on the flow rates in the tubes. Stopwatch was used to record the times to drain 150 g (150.3 ml) of water through the SHB and corresponding control capillaries. The experiment was performed three times with each diameter of capillary to estimate the average flow rate to calculate the Reynolds number of each capillary's flow. The reported values are the averages plus-minus standard deviations. The Reynolds number was calculated with equation 6 with fluid viscosity of 1.003 mPa.s and water density of 998 kg/m^3.

6 Results and Discussions

6.1 Surface Characterization

6.1.1 Film Thickness

The ALD Al_2O_3 film thickness measured by ellipsometry are presented in Table 1, along with the Al_2O_3 nanograss thicknesses after the hydrothermal treatment (HTT). These measurements were done with two monitor Si wafer samples from three different batches.

Table 1: Thicknesses of Al_2O_3 film and Al_2O_3 nanograss. These are Al_2O_3 thicknesses from before and after hydrothermal treatment (HTT) of the two monitor Si wafers from three fabrication batches.

Batch		**Al_2O_3 film Thickness (nm)**	**Al_2O_3 Nanograss Thickness (nm)**
1	**Inlet**	26.50	122.60
	Outlet	24.70	118.20
2	**Inlet**	26.40	123.00
	Outlet	25.90	122.00
3	**Inlet**	25.90	120.00
	Outlet	24.80	117.00

The resultant average Al_2O_3 film thickness at the inlet before hydrothermal treatment (HTT) is 26. 23 ± 0.32 nm, which grows to an average of 122.53 ± 0.50 nm Al_2O_3 nanograss after the HTT. Similarly, the average thickness at the outlet is 25.13 ± 0.67 nm, which grows to an average of 119.07 ± 2.61 nm. Therefore, a gradient of 25.68 ± 0.78 nm Al_2O_3 film thickness was formed on the inner walls of the capillaries. This grew to an estimated 120.80 ± 2.45 nm gradient of Al_2O_3 nanograss after the HTT. This is consistent with the referenced literature as Kauppinen and co-workers [63] recorded 28 nm as the Al_2O_3 film thickness, which increased to 125 nm thick nanograss layer after HTT.

The refractive index of the Al_2O_3 film was about 1.68 ± 0.3, which decreased to 1.20 ± 0.01 with the formation of the Al_2O_3 nanograss after the HTT. This is also consistent when compared to the referenced literature, Kauppinen and co-workers [63] reported the initial refractive index of Al_2O_3 film as 1.64, which reduced to 1.20.

6.1.2 Transparency

Figure 24 is a set of images of the control (as received) capillaries (A) and the SHB capillaries (B). It could be observed with the unaided eye that both sets of capillaries are transparent enough to be seen through. This is evident in the clear showing of the text captions under both the control (Figure 24A) and SHB (Figure 24B) capillaries. Therefore, the SHB fabricated layer from the adopted fabrication approach does not compromise the transparency of the substrate. This feature makes the fabricated SHB capillaries applicable in fluid transfers where optical observation of fluid flow is necessary.

Figure 24: Optical appearances of the two sets of capillaries: (A) Control (as received) set of 100 mm long capillaries and (B) SHB capillaries 100 mm long capillaries. Both sets of capillaries appear transparent as the text captions beneath them can be clearly seen.

6.1.3 Surface Morphology by SEM

Figure 25 shows the SEM micrograph of the formed nano-grass on the reference Si planar sample. It shows the fabrication process adopted produced the desired micro-nano grass-like physical appearance of the hierarchical structures on the surface.

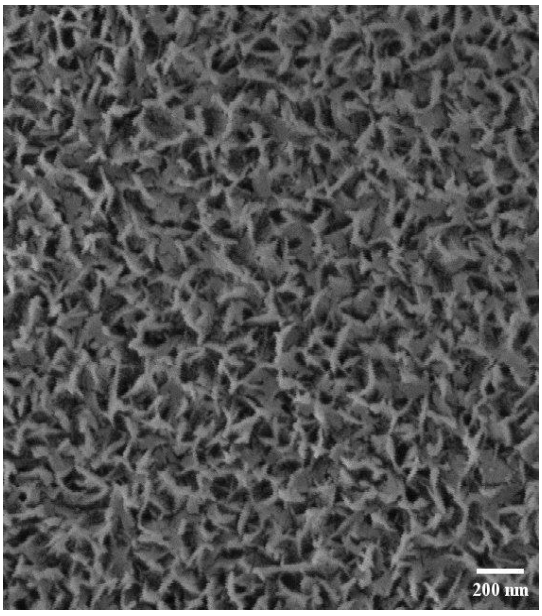

Figure 25: SEM micrograph of the appearance of the Al_2O_3 on the reference planar Si wafer. The fabrication of the Al_2O_3 layer on this planar wafer was simultaneously done with the glass capillaries.

The features of the deposited Al_2O_3 layer on the inner walls of the glass capillaries are shown in the SEM micrographs of Figure 26. The features from the largest glass capillary (ID-6) are seen in Figure 26A (20 mm section from one end) and B (middle 20 mm section). It can be observed that the micro-nano grass structures seen on the monitor planar Si (Figure 25) appears like the structures seen on both cut sections of the capillary. This implies that the fabrication method adopted was successful in creating Al_2O_3 nanograss on the total surface area of the inner walls of capillary with aspect ratio of about 17 (100 mm long with 6 mm inner diameter).

The Al_2O_3 nanograss features on glass capillary with inner diameter 4 mm is shown in Figure 26C (20 mm section from one end) and D (middle 20 mm

section). The features are also like the Al_2O_3 grown features on the monitor planar Si surface in Figure 25. This indicates the successful fabrication of Al_2O_3 nanograss on the total surface area of the inner walls of glass capillary with aspect ratio of 25 (100 mm long with 4 mm inner diameter).

Figure 26E (20 mm section from one end) and F (middle 20 mm section) are the SEM micrographs of the Al_2O_3 grown layer on the 100 mm long smallest tube of 0.6 mm inner diameter. It can be observed that the Al_2O_3 nanograss features on the 20 mm section from one end of the capillary (Figure 26E) is like the features on the planar Si monitor surface. However, the features from the 20 mm middle section (Figure 26F) appear a relatively homogeneous film layer, depicting the original Al_2O_3 film deposited during the ALD step. Evidently, the ALD step was successful in depositing the Al_2O_3 film on the total inner surface area of a capillary with aspect ratio of about 167 (100 mm long with 0.6 mm inner diameter). However, the hydrothermal treatment was not able to form nanograss in the tubes with aspect ratio of about 167.

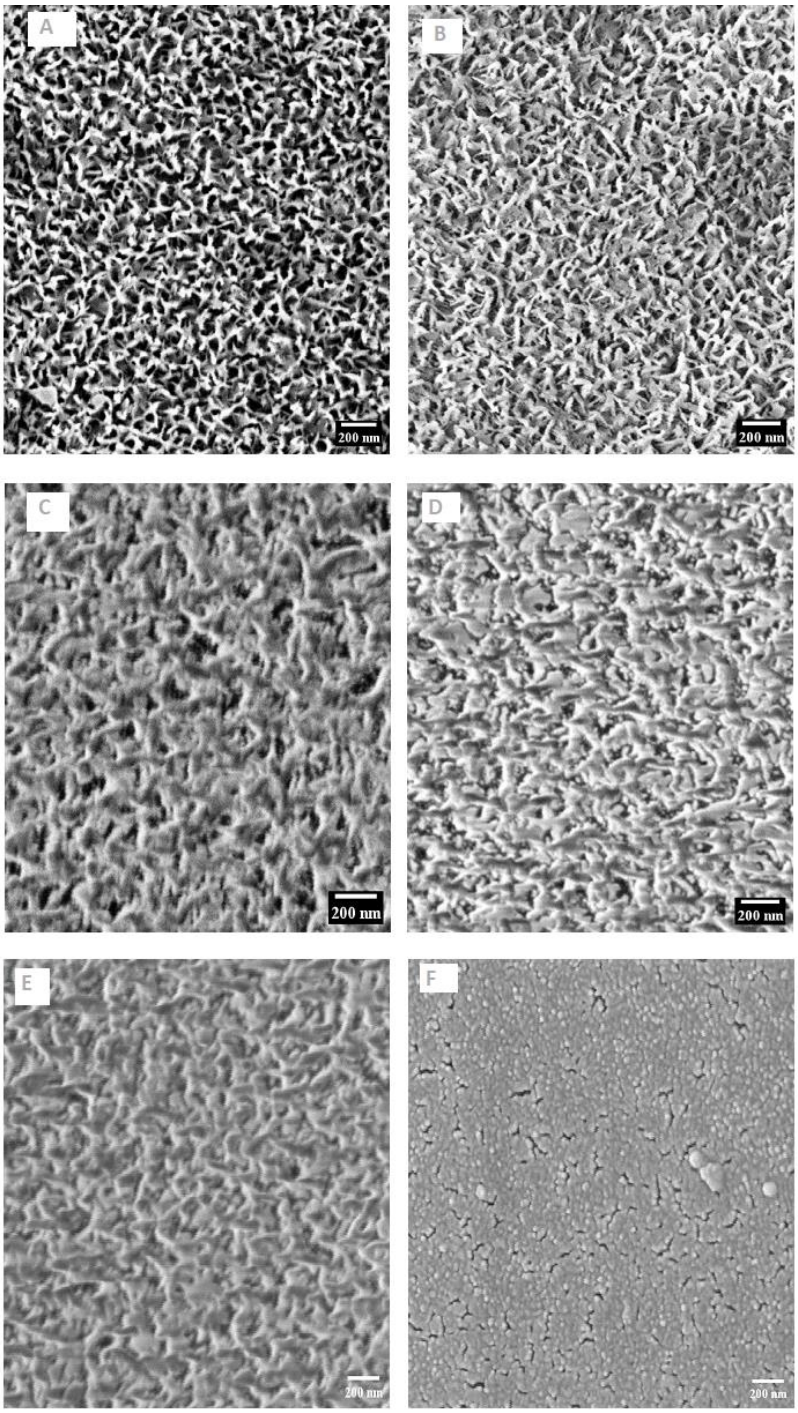

Figure 26: SEM micrographs (all with 200 nm scale bar) of the Al_2O_3 coated layers on the inner walls of the three different capillary diameters. The micrographs on the left side are from one end of the capillaries, while the micrographs on the right are from the mid-sections of the 100 mm long capillaries. (A) is end and (B) is mid-section of ID-6 capillary, (C) is end and (D) is mid-section of ID-4 capillary, (E) is end and (F) is mid-section cut of ID-0.6 capillary.

6.1.4 Contact Angle Results

Figure 27 shows an image each from the advancing CA measurement (A) and receding CA measurement (B) on the planar Si wafer sample with water droplet. The resulting average advancing CA is just above 169° and the average receding angle over 168°. This resulted in a CA hysteresis <1 degree. As stated earlier [1-5, 8], CA of over 150° with CA hysteresis less than 5° indicate the successful fabrication of SHB surfaces on the samples.

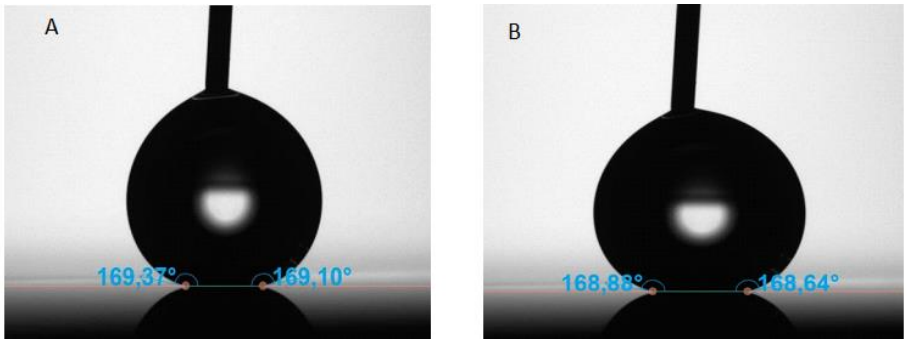

Figure 27: Images of CA on planar Si sample with water droplet: (a) Advancing CA and (b) Receding CA.

The result indicates that the modification of the surface of the rough micro-nano flower-like structures by the SAM treatment resulted in reduction of the surface energy. As discussed in the earlier sections, the surface roughness provided by the micro-nano structural growth of the ALD and hydrothermal treatment of Al_2O_3 leads to a decrease in the area fraction of the surface of the silicon and glass capillary by the grown Al_2O_3 micro-nano roughness. This leads to air entrapment between the Al_2O_3 protrusions, which forms a barrier between the water droplet and the substrate surface. Also, the low surface energy provided by the SAM functionalization leads to low surface adhesion between the liquid droplet and the solid surface, satisfying a Cassie-Baxter wetting model with a low CA hysteresis (<1 degree).

6.2 Fluidic Performance

6.2.1 Droplet Sliding Angle

The average water droplet sliding angles (SA) of SHB glass capillaries and untreated (control) capillaries for the different diameter capillaries at 100 mm lengths are reported in Table 2. From the results in Table 2, it can be deduced that the SHB coating in the treated capillaries greatly influence the sliding angles relative to their control counterparts, producing over 7 times ratio of improvement.

Table 2: Average sliding angle performance and respective standard deviations of 100 mm long SHB capillaries versus control tubes.

Capillary ID (mm)	**Droplet volume (µL)**	**Water Sliding Angle (˚)**		**Improvement Ratio**
		SHB	Control	
6	500	2.5 ± 0.1	18.0 ± 0.5	7.2
4	200	6.2 ± 0.3	52.3 ± 0.6	8.4
0.6	35	46.3 ± 0.6	N. A	N. A

The SHB capillary with the biggest diameter or inner diameter 6 mm (ID-6) produced the lowest average droplet sliding angle. According to equation 10, the large diameter of this capillary results in a larger driving force to initiate sliding of the water droplet over the SHB surface. Also, the CA hysteresis is lowest in the ID-6 capillary relative to its corresponding control capillary. Therefore, there is little activation barrier (see equation 9) to be overcome by the spherical droplet shape change through tilting. This also implies the ID-6 has the lowest increase in liquid-vapor interface area. Thus, it requires the lowest activation barrier to cause water droplet to transition from one ground stat to another.

The SHB capillary with inner diameter 4 (ID-4) showed a higher average droplet sliding angle as compared to that of ID-6. This is consistent with reference [61], because the smaller inner diameter of ID-4 relative to ID-6 implies that, it has lower driving force to initiate the sliding of the droplet. The water droplet required bigger change in droplet shape through tilting to overcome a higher activation barrier. The control ID-4 had higher average droplet SA because it has higher CA hysteresis, and therefore requires higher droplet shape change through tilting, to compensate for the higher activation energy.

Finally, the SHB capillary with the smallest diameter or inner diameter 0.6 (ID-0.6) produced the highest average droplet sliding angle, which is also suggestive of a resultant small driving force to initiate water droplet sliding because of its small diameter. This implies that ID-0.6 required the most change in droplet shape through the highest tilting to overcome the highest activation barrier. The droplet in control capillary did not drop out of the capillary even at 90°. This is due to inadequate room to generate adequate activation energy through droplet shape change. activation barrier of the untreated surface was high, but the droplet did not have enough space, because of its small diameter, to change shape to gain enough activation energy to overcome the surface activation barrier.

6.2.2 Bio-Repellency

The result of the droplet sliding angle (SA) with different concentrations of protein solution BSA in PBS is tabulated in Table 3 below. From the result, it can be observed that the SHB capillaries provide substantial drag reduction within an improvement factor in the range of 5-3 with the largest capillaries (ID-6), and 6 – 2 with ID-4 capillaries. This is attributed to the features of the SHB layer, which are rough hierarchical structures with air pockets and low surface energy from the silane coating. This is in agreement with literature [66], where BSA has been demonstrated to be adsorbed more on to SHB surfaces with large roughness features, but adsorbed much less on to SHB surface with small roughness features with more entrapped

air. These conditions provide low activation barrier for the droplet, and hence lesser need for change of droplet shape through increase in tilting angle before sliding of the droplet [61].

Table 3: Results of the average droplet sliding angles of protein solution BSA dissolved in PBS, along with their standard deviations. The droplet volumes of the protein solutions were the same as the water droplet volumes.

Capillaries	**SA (˚) with 2 µg/ml BSA**	**SA (˚) with 20 µg/ml BSA**	**SA (˚) with 200 µg/ml BSA**
SHB – ID-6	3.5 ± 0.1	5.0 ± 0.1	11.2 ± 0.2
CONTROL – ID-6	18.2 ± 0.3	23.2 ± 0.3	31.2 ± 0.3
Improvement Ratio	5.2	4.6	2.8
SHB – ID-4	8.5 ± 0.1	22.0 ± 0.1	33.0 ± 0.2
CONTROL – ID-4	52.0 ± 0.5	55.0 ± 0.5	57.0 ± 0.5
Improvement Ratio	6.1	2.5	1.7
SHB – ID-0.6	50.0 ± 0.5	68.0± 0.5	N. A
CONTROL – ID-0.6	N. A	N. A	N. A

The lower SA from the largest diameter (ID-6) also indicate the highest level of superhydrophobicity because it has best aspect-ratio for the fabrication steps adopted. Its greater SHB features implies it has the lowest CA hysteresis to support droplet sliding at the lowest sliding angle, which is consistent with literature [11, 61].

On the contrary, the SHB ID-0.6 capillary exhibited the highest SA angles in general, because of the relatively poor SHB coat leading to higher CA hysteresis. The droplet of the highest concentration biological fluid did not slide out of even the SHB capillary. This implies high surface energy of the capillary surface leading to strong adhesion force with the droplet, which leads to Wenzel's wetting mode of the capillary surface. Also, the higher

density of the highest concentration droplet increases the droplet's tendency to flatten because of the higher gravitational force.

Droplet of all the BSA concentrations did not slide out of untreated ID-0.6 capillary at any angle. This is attributed to an extremely high CA hysteresis of the surface which did not permit sliding. Also, the high surface energy of due to inadequate air pocket formation on the capillary surface leads to high adhesion force between the liquid droplet and surface.

6.2.3 Hydraulic Drag Resistance and Reynolds Number

The average volumetric flow rates (AFR) to drain 150.3 ml (150 g) of DIW through the 100 mm long capillaries at the different hydrostatic pressure or water height (WH) and their corresponding Reynolds numbers (Re) are presented in Table 4 below. The results are experiments with the experimental setup in Figure 23.

Table 4: The average volumetric flow rates (AFR) with their standard deviations from the 100 mm long SHB capillaries and their respective controls and their corresponding Reynolds number (Re).

Glass capillaries		**AFR at WH 68.5 cm ($10^{-6}m^3/s$)**	**Re**	**AFR at WH 34.0 cm ($10^{-6}m^3/s$)**	**Re**	**AFR at WH 17.0 cm ($10^{-6}m^3/s$)**	**Re**
ID-6	SHB	22.60 ± 0.1	4800	15.30 ± 0.07	3200	10.51 ± 0.06	2200
	Control	21.84 ± 0.2	4600	14.71 ± 0.08	3100	10.16 ± 0.05	2100
ID-4	SHB	8.85 ± 0.08	2800	5.95 ± 0.04	1900	4.02 ± 0.005	1300
	Control	8.31 ± 0.07	2600	5.61 ± 0.03	1800	3.80 ± 0.01	1200
ID-0.6	SHB	0.73 ± 0.0006	1500	0.48 ± 0.0001	1000	0.25 ± 0.00002	500
	Control	0.77 ± 0.0001	1600	0.47 ± 0.00005	1000	0.14 ± 0.00003	300

From the results it can be deduced that, the ID-6 capillaries exhibited turbulent flow regimes (>4000) at the highest water levels. However, they exhibited transitional flow regime (2300 – 4000) at lower water height. The ID-4 capillaries exhibited transitional flow regime at the highest water level and laminar flow regimes (<2300) at lower water heights. The ID-0.6 capillaries exhibited laminar flow regimes at all the water levels. [49, 50].

The results also indicate that the flow rates within the SHB capillaries and thus the Re are higher than their respective control capillaries in the range of 3 – 6% for ID-6 and ID-4 capillaries over the 3 hydrostatic pressures. This is consistent the with concept that SHB layer introduces reduction of frictional resistance between the liquid-solid interface to promote slip length and slip velocity of flowing fluid to increase flow rates [51, 54, 55].

The hydrostatic pressure as a result of the different water height greatly influenced the general flow behaviour. This is observed (see Table 4) by the turbulent flows in both ID-6 capillaries at 68.5 cm of WH, transitional flows at 34.0 cm WH and laminar flows at 17.0 cm WH. The ID-4 capillaries exhibit transitional flows at the highest WH and laminar flows at both intermediate and lowest WH.

The ID-0.6 capillaries exhibit laminar flows at all the hydrostatic pressures, which is due to the small volumetric flow rate as result of the small diameter. Again, the SHB capillary of ID-0.6 showed substantial improvement in flow rate at the lowest hydrostatic pressure, of about 43% drag reduction relative to the control capillary. This is because the SHB surface on the treated capillary provides lower CA hysteresis that reduces the activation barrier to be overcome by the flowing water. This implies higher drag reduction is achieved at low Reynolds number. This phenomenon is consistent with literature [7, 60]. Also, the low hydrostatic pressure (see equation 7) exerted by the water in the reservoir implies that the flowing water possessed significant force to push the water particles to penetrate the air-pockets [56, 59], but instead the SHB features provided adequate slip flow over the SHB layer.

7 Conclusions and Future Outlook

The inner walls of glass capillaries have been coated with a superhydrophobic layer through a three-step fabrication approach: ALD, hydrothermal treatment and silane deposition. The fabrication was done on the inner walls of three different capillaries at 100 mm long with inner diameters 6 mm, 4 mm and 0.6 mm. The average thickness of the ALD Al_2O_3 film on the inner walls of the capillaries was 25.68 ± 0.78 nm. The Al_2O_3 nanograss formation during the hydrothermal treatment increased the average layer thickness to an estimated 120.80 ± 2.45 nm. The advancing CA of the SHB layer measured with a monitor planar Si wafer was >169° and receding CA >168°, with a resultant CA hysteresis <1°.

SEM characterization indicated successful Al_2O_3 nano grass-like formation on the total inner surface area of both 6 mm and 4 mm inner diameter capillaries. Also, the first 20 mm sections of both ends of the capillary with inner diameter 0.6 mm exhibited formation of the desired nanograss structures. The features of the nanograss on the inner walls of the capillaries are comparable to the nanograss grown on the monitor planar Si wafer samples. However, the 20 mm middle section only exhibited the Al_2O_3 film deposited at the ALD step. This indicates that the hydrothermal treatment, as adopted in this fabrication approach, was not effective to cause Al_2O_3 nanograss formation at aspect ratio of about 167.

Fluidic performance evaluation indicated that the SHB capillaries produced lower sliding angles (improvement by a factor of seven) relative to their controls due to the introduction of drag reduction by the SHB layer. Also, the bigger the capillary diameter produced the lowest droplet sliding angle. This was due to an increasing driving force; that initiates droplet sliding, with increasing diameter. The fabricated SHB capillaries also exhibited bio-repellency as they produced smaller droplet sliding angles with droplet of protein solution BSA.

The SHB capillaries also produced higher water flow rates resulting in larger Reynolds numbers. It has been demonstrated that at lower Reynolds number, bigger drag reduction is achieved. Therefore, the SHB capillaries

can be applied in fluid transfers to facilitate lossless transfers and provide drag reduction to enhance energy cost efficiency in fluid transfers. The SHB capillaries are also transparent, which makes them potentially viable for fluidic transfer applications which require observation of fluid flow, such as fluid transfusions in health delivery system.

Further investigations are required to determine which parameters of the hydrothermal treatment, either the temperature settings (85 – 90°C) or immersion time (30 minutes), prevents the nanograss growth in ID-0.6 mm (aspect ratio of 167) capillary. Also, further tests are required to determine the robustness and chemical durability of this SHB layer. For instance, experiments such as mechanical erosion testing and antibacterial activity experiment among others can promote the range of practical application of the Al_2O_3 nanograss SHB layer in health delivery system.

8 References

1. Bhushan, B. and Y.C. Jung, *Natural and biomimetic artificial surfaces for superhydrophobicity, self-cleaning, low adhesion, and drag reduction.* Progress in Materials Science, 2011. **56**(1): p. 1-108.

2. Chu, F., *Condensed and melting droplet behavior on superhydrophobic surfaces*. 1st 2020. ed. Springer theses. 2020, Singapore: Tsinghua University Press.

3. Wang, D., et al., *Design of robust superhydrophobic surfaces.* Nature, 2020. **582**(7810): p. 55-59.

4. Kim, S.H., *Fabrication of Superhydrophobic Surfaces.* Journal of Adhesion Science and Technology, 2008. **22**(3-4): p. 235-250.

5. Zhu, T., et al., *A transparent superhydrophobic coating with mechanochemical robustness for anti-icing, photocatalysis and self-cleaning.* Chemical Engineering Journal, 2020. **399**: p. 125746.

6. Isakov, K., et al., *Superhydrophobic Antireflection Coating on Glass Using Grass-like Alumina and Fluoropolymer.* ACS Applied Materials & Interfaces, 2020. **12**(44): p. 49957-49962.

7. Hoshian, S., et al., *Water and Blood Repellent Flexible Tubes.* Scientific Reports, 2017. **7**(1): p. 16019.

8. Parvate, S., P. Dixit, and S. Chattopadhyay, *Superhydrophobic Surfaces: Insights from Theory and Experiment.* The Journal of Physical Chemistry B, 2020. **124**(8): p. 1323-1360.

9. Yuan, J.-J. and R.-H. Jin, *Water motion and movement without sticking, weight loss and cross-contaminant in superhydrophobic glass tube.* Nanotechnology, 2010. **21**(6): p. 065704.

10. Vuckovac, M., et al., *Viscosity-enhanced droplet motion in sealed superhydrophobic capillaries.* Science Advances, 2020. **6**(42): p. eaba5197.

11. Gao, L. and T.J. McCarthy, *Contact Angle Hysteresis Explained.* Langmuir, 2006. **22**(14): p. 6234-6237.

12. Cassie, A.B.D. and S. Baxter, *Wettability of porous surfaces.* Transactions of the Faraday Society, 1944. **40**(0): p. 546-551.

13. Zhi, J. and L.Z. Zhang, *Durable superhydrophobic surfaces made by intensely connecting a bipolar top layer to the substrate with a middle connecting layer.* Sci Rep, 2017. **7**(1): p. 9946.

14. Tavana, H., A. Amirfazli, and A.W. Neumann, *Fabrication of Superhydrophobic Surfaces of n-Hexatriacontane.* Langmuir, 2006. **22**(13): p. 5556-5559.

15. Mattox, D.M., *Handbook of physical vapor deposition (PVD) processing*. 2nd ed. 2010, Amsterdam: Elsevier.

16. Sahin, F., et al., *Antifouling superhydrophobic surfaces with bactericidal and SERS activity.* Chemical Engineering Journal, 2022. **431**: p. 133445.

17. Cardoso, J.T., et al., *Superhydrophobicity on hierarchical periodic surface structures fabricated via direct laser writing and direct laser interference patterning on an aluminium alloy.* Optics and Lasers in Engineering, 2018. **111**: p. 193-200.

18. Tanvir Ahmmed, K.M. and A.-M. Kietzig, *Drag reduction on laser-patterned hierarchical superhydrophobic surfaces.* Soft Matter, 2016. **12**(22): p. 4912-4922.

19. S.C, V., et al., *Laser patterned titanium surfaces with superior antibiofouling, superhydrophobicity, self-cleaning and durability: Role of line spacing.* Surface and Coatings Technology, 2021. **418**: p. 127257.

20. Nguyen, H.H., et al., *Surface characteristics and wettability of superhydrophobic silanized inorganic glass coating surfaces textured with a picosecond laser.* Applied Surface Science, 2021. **537**: p. 147808.

21. Donnelly, T., G. O'Connell, and J.G. Lunney *Metal Nanoparticle Film Deposition by Femtosecond Laser Ablation at Atmospheric Pressure*. Nanomaterials, 2020. **10**, DOI: 10.3390/nano10112118.

22. Darmanin, T., et al., *Superhydrophobic Surfaces by Electrochemical Processes.* Advanced Materials, 2013. **25**(10): p. 1378-1394.

23. Song, J.-l., et al., *Electrochemical machining of super-hydrophobic Al surfaces and effect of processing parameters on wettability.* Applied Physics A, 2012. **108**(3): p. 559-568.

24. Vistas, C.R., A.C.P. Águas, and G.N.M. Ferreira, *Silanization of glass chips—A factorial approach for optimization.* Applied Surface Science, 2013. **286**: p. 314-318.

25. Jin, R.-H. and J.-J. Yuan, *Biomimetically Controlled Formation of Nanotextured Silica/Titania Films on Arbitrary Substrates and Their Tunable Surface Function.* Advanced Materials, 2009. **21**(37): p. 3750-3753.

26. Zhang, L., et al., *Functional and versatile superhydrophobic coatings via stoichiometric silanization.* Nature Communications, 2021. **12**(1): p. 982.

27. Zhu, D., N. Hu, and D.W. Schaefer, *Chapter 1 - Water-based sol–gel coatings for military coating applications*, in *Handbook of Waterborne Coatings*, P. Zarras, M.D. Soucek, and A. Tiwari, Editors. 2020, Elsevier. p. 1-27.

28. Tasaltin, N., et al., *Preparation and characterization of superhydrophobic surfaces based on hexamethyldisilazane-modified nanoporous alumina.* Nanoscale Research Letters, 2011. **6**(1): p. 487.

29. Montgomerie, Z. and K.C. Popat, *Improved hemocompatibility and reduced bacterial adhesion on superhydrophobic titania nanoflower surfaces.* Materials Science and Engineering: C, 2021. **119**: p. 111503.

30. Huang, S., et al., *Superhydrophobic micro-tube fabricated via one-step plasma polymerization for lossless droplet transfer.* Surface and Coatings Technology, 2021. **421**: p. 127272.

31. Odian, G.G., *Principles of polymerization*. 4th ed. 2004, Hoboken, N.J: Wiley-Interscience.

32. Liu, C., C.-Y. Hong, and C.-Y. Pan, *Polymerization techniques in polymerization-induced self-assembly (PISA).* Polymer Chemistry, 2020. **11**(22): p. 3673-3689.

33. Kim, S., H. Cho, and W. Hwang, *Simple fabrication method of flexible and translucent high-aspect ratio superhydrophobic polymer tube using a repeatable replication and nondestructive detachment process.* Chemical Engineering Journal, 2019. **361**: p. 975-981.

34. Li, J., et al., *One-Step Spray-Coating Process for the Fabrication of Colorful Superhydrophobic Coatings with Excellent Corrosion Resistance.* Langmuir, 2015. **31**(39): p. 10702-10707.

35. Maghsoudi, K., et al., *Direct replication of micro-nanostructures in the fabrication of superhydrophobic silicone rubber surfaces by compression molding.* Applied Surface Science, 2018. **458**: p. 619-628.

36. Xiang, T., et al., *Fabrication of Inherent Anticorrosion Superhydrophobic Surfaces on Metals.* ACS Sustainable Chemistry & Engineering, 2018. **6**(4): p. 5598-5606.

37. Zhou, J., et al., *Electroplating of non-fluorinated superhydrophobic Ni/WC/WS2 composite coatings with high abrasive resistance.* Applied Surface Science, 2019. **487**: p. 1329-1340.

38. Giurlani, W., et al. *Electroplating for Decorative Applications: Recent Trends in Research and Development*. Coatings, 2018. **8**, DOI: 10.3390/coatings8080260.

39. Ling, Y.D. and S. Torii, *Heat transfer enhancements in heat pipe constructed with a copper porous microstructure.* International Journal of Green Energy, 2021. **18**(2): p. 166-171.

40. Iacovetta, D., J. Tam, and U. Erb, *Synthesis, structure, and properties of superhydrophobic nickel–PTFE nanocomposite coatings made by electrodeposition.* Surface and Coatings Technology, 2015. **279**: p. 134-141.

41. Asiabi, H., et al., *Electroplating of nanostructured polyaniline–polypyrrole composite coating in a stainless-steel tube for on-line in-tube solid phase microextraction.* Journal of Chromatography A, 2015. **1397**: p. 19-26.

42. Kaariainen, T., et al., *Atomic layer deposition principles, characteristics, and nanotechnology applications*. 2nd ed. 2013, Hoboken, NJ: John Wiley & Sons.

43. Masse de la Huerta, C., et al. *Influence of the Geometric Parameters on the Deposition Mode in Spatial Atomic Layer Deposition: A Novel Approach to Area-Selective Deposition*. Coatings, 2019. **9**, DOI: 10.3390/coatings9010005.

44. Xiao, X., et al., *Durable superhydrophobic wool fabrics coating with nanoscale Al2O3 layer by atomic layer deposition.* Applied Surface Science, 2015. **349**: p. 876-879.

45. Li, Y., et al., *Micro/Nano hierarchical peony-like Al doped ZnO superhydrophobic film: The guiding effect of (100) preferred seed layer.* Scientific Reports, 2016. **6**(1): p. 19187.

46. Baruah, S. and J. Dutta, *Hydrothermal growth of ZnO nanostructures.* Science and Technology of Advanced Materials, 2009. **10**(1): p. 013001.

47. Zhu, C., et al., *Atomic Layer Deposition of TiO2 Thin Films on the Inner Walls of Steel Tubes Increases Anti-coking Properties.* ACS Omega, 2020. **5**(49): p. 32102-32111.

48. Puurunen, R.L., *Growth Per Cycle in Atomic Layer Deposition: A Theoretical Model.* Chemical Vapor Deposition, 2003. **9**(5): p. 249-257.

49. Kamand Fadi, Z., *Hydraulic Friction Factors for Pipe Flow.* Journal of Irrigation and Drainage Engineering, 1988. **114**(2): p. 311-323.

50. Kiijarvi, J., *Darcy friction factor formulae in turbulent pipe flow.* Lunowa Fluid Mechanics Paper, 2011. **110727**(2011): p. 1-11.

51. Yan, H., et al., *Durable drag reduction and anti-corrosion for liquid flows inside lubricant-infused aluminum/copper capillaries.* Chemical Engineering Science, 2023. **266**: p. 118275.

52. Amromin, E., *Capillary Waves Joint to Super-Hydrophobic Bars.* Journal of Fluids Engineering, 2019. **141**(11).

53. Kim, Y.W., et al., *Skin friction reduction in tubes with hydrophobically structured surfaces.* International Journal of Precision Engineering and Manufacturing, 2013. **14**(2): p. 299-306.

54. Tabeling, P., *A brief introduction to slippage, droplets and mixing in microfluidic systems.* Lab on a Chip, 2009. **9**(17): p. 2428-2436.

55. Shashi Menon, E., *Chapter Five - Fluid Flow in Pipes*, in *Transmission Pipeline Calculations and Simulations Manual*, E. Shashi Menon, Editor. 2015, Gulf Professional Publishing: Boston. p. 149-234.

56. Extrand, C.W., *Origins of Wetting.* Langmuir, 2016. **32**(31): p. 7697-7706.

57. Dasaev, M., et al. *On the reduction of hydraulic resistance based on the hydrophobization of functional surfaces*. in *Journal of Physics: Conference Series*. 2021. IOP Publishing.

58. Daniello, R.J., N.E. Waterhouse, and J.P. Rothstein, *Drag reduction in turbulent flows over superhydrophobic surfaces.* Physics of Fluids, 2009. **21**(8): p. 085103.

59. Liravi, M., et al., *A comprehensive review on recent advances in superhydrophobic surfaces and their applications for drag reduction.* Progress in Organic Coatings, 2020. **140**: p. 105537.

60. Hurst, E., Q. Yang, and Yongmann M. Chung, *The effect of Reynolds number on turbulent drag reduction by streamwise travelling waves.* Journal of Fluid Mechanics, 2014. **759**: p. 28-55.

61. Papadopoulou, E., et al., *Nanopumps without Pressure Gradients: Ultrafast Transport of Water in Patterned Nanotubes.* The Journal of Physical Chemistry B, 2022. **126**(3): p. 660-669.

62. VWR. *Glass tubing*. 2022 [cited 2022 5 November 2022]; Available from: https://fi.vwr.com/store/product/577771/glass-tubing.

63. Kauppinen, C., K. Isakov, and M. Sopanen, *Grass-like Alumina with Low Refractive Index for Scalable, Broadband, Omnidirectional Antireflection Coatings on Glass Using Atomic Layer Deposition.* ACS Applied Materials & Interfaces, 2017. **9**(17): p. 15038-15043.

64. Aldrich, S. *1H,1H,2H,2H-Perfluorododecyltrichlorosilane*. [cited 2022; Available from: https://www.sigmaaldrich.com/FI/en/product/aldrich/729965?gclid=Cj0KCQiAvqGcBhCJARIsAFQ5ke6tQ9TU_EcF5P99bepDkFuIruILUdGmSvXdqOpRsiGmJrl5L2SGztEaAgeCEALw_wcB&gclsrc=aw.ds.

65. Brand, F.S.A.T.F.S. *Thermo Scientific™ Bovine Serum Albumin (BSA)*. 2022 [cited 2022 20.11.2022]; Available from: https://www.fishersci.fi/shop/products/fermentas-bovine-serum-albumin-bsa/10829410?searchHijack=true&searchTerm=10829410&searchType=RAPID&matchedCatNo=10829410.

66. Falde, E.J., et al., *Superhydrophobic materials for biomedical applications.* Biomaterials, 2016. **104**: p. 87-103.